

# Rectifying bedload flux variability from channel geometry and grain shape effects

Thomas Pächt,<sup>1,2\*†</sup> Yulan Chen,<sup>1†</sup> Jiafeng Xie,<sup>1,3</sup> Rémi Monthiller,<sup>4</sup>  
 Raphaël Maurin,<sup>5</sup> Katharina Tholen,<sup>6</sup> Yen-Cheng Lin,<sup>7</sup> Hao-Che Ho,<sup>7</sup>  
 Peng Hu,<sup>1\*</sup> Zhiguo He,<sup>1\*</sup> Orencio Durán<sup>8</sup>

<sup>1</sup>Institute of Port, Coastal and Offshore Engineering, Ocean College, Zhejiang University,  
 316021 Zhoushan, China

<sup>2</sup>Donghai Laboratory, 316021 Zhoushan, China

<sup>3</sup>State Key Laboratory of Fluid Power and Mechatronic Systems and Department of  
 Engineering Mechanics, Zhejiang University, Hangzhou 310027, China

<sup>4</sup>Aix-Marseille University, CNRS, Centrale Marseille, Institut de Recherche sur les  
 Phénomènes Hors Équilibre (IRPHÉ), Marseille 13384, France

<sup>5</sup>Institut de Mécanique des Fluides de Toulouse (IMFT), Université de Toulouse,  
 CNRS, F-31400 Toulouse, France

<sup>6</sup>Institute for Theoretical Physics, Leipzig University, Postfach 100920, 04009 Leipzig, Germany

<sup>7</sup>Department of Civil Engineering, National Taiwan University, Taipei City 106, China

<sup>8</sup>Department of Ocean Engineering, Texas A&M University, College Station,  
 Texas 77843-3136, USA

\*Corresponding author. E-mail: 0012136@zju.edu.cn (T.P.); pengphu@zju.edu.cn (P.H.);  
 hezhiguo@zju.edu.cn (Z.H)

† These authors contributed equally to this work.

**Bedload transport occurs when a bed composed of sedimentary grains becomes mobile in response to the shearing by a flow of liquid. It shapes the landscapes of Earth and other planetary bodies by promoting the formation and growth of various multiscale geological features. Estimating the rate at**

which such processes take place requires accurate bedload flux predictions. However, even for highly idealized conditions in the laboratory, study-to-study variability of reported bedload flux measurements borders an order of magnitude. This uncertainty stems from physically poorly supported, typically empirical methods to account for channel geometry effects in the determination of the transport-driving bed shear stress and from study-to-study grain shape variations. Here, we derive and validate a universal method of bed shear stress determination and apply it to a number of independent grain-shape-controlled data sets from experiments and CFD-DEM simulations for a very diverse range of transport conditions. An existing physical bedload flux model, here generalized to account for grain shape variability, predicts almost all these data within a factor of 1.3, whereas a recently proposed grain shape correction of the bed shear stress (Deal et al., *Nature* 613, 298-302, 2023) substantially increases the bedload flux scatter across weak and intense transport conditions.

**Teaser** This study rectifies two important causes for the large study-to-study variability of reported bedload flux measurements.

## Introduction

Bedload transport is a special kind of sediment transport in which typically coarse sedimentary grains roll, slide, and hop along the surface in response to the shearing of a loose granular bed by a flow of liquid. It plays a vital role in shaping the environments of Earth and other planetary bodies (1) by promoting the formation and growth of geological features of various scales, including ripples and dunes (2, 3), deltas and fans (4), and laminations and cross-bedding (5, 6).

A key problem hampering our understanding of bedload-induced landscape evolution is the notoriously large noise commonly associated with measurements of bedload flux, often exceeding an order of magnitude (7, 8). It partially originates from huge non-Gaussian flux fluctuations over large time scales, which even occur under steady flow conditions in the laboratory due to continuous topographic change (9). However, also when restricted to steady flows over flat beds at short timescales, reported bedload fluxes can still substantially differ between laboratory studies for largely self-similar conditions, for both weak and intense transport-driving flows (8), and it has been unclear whether such differences arise due to physical or experimental reasons. On the one hand, physical reasons may come into play because dissimilarities in grain size and shape distributions are not accounted for by commonly used similarity parameters. On the other hand, study-to-study variability of the geometry of laboratory facilities is a potential culprit on the experimental side, especially in view of the associated large random and systematic uncertainties in the experimental determination of the transport-driving bed shear stress (10). Focusing here on rectangular open channels, since they are geometrically similar to natural streams, the ratio  $b/h$  between the channel width  $b$  and flow depth  $h$  is a crucial parameter in this regard. Ideally, one would want  $b/h$  to be as large as possible to most closely resemble bedload transport in nature. However, in experimental reality,  $b/h$  is often of order unity, substantially weakening the shearing of the bed due to frictional losses at the sidewalls, causing the flow to be nonuniform in the cross-channel direction (11).

In an attempt to understand the origin of bedload flux variability in nature, Zhang et al. (12, 13) conducted grain-resolved numerical simulations of steady state gravel transport by turbulent water flow in which they varied a number of control parameters, including grain shape, and studied their effects on bedload flux. Furthermore, almost the same authors, Deal et al. (14), carried out laboratory experiments to measure bedload flux for various grain shapes. Based on their numerical and experimental data, they concluded that grain shape is a key contributor to

bedload flux variability and derived a semiempirical bedload flux model correcting for grain shape effects. However, since these data were solely obtained from laboratory and numerical experiments in a deep and very narrow channel ( $b/h \approx 10^{-1}$ ), merely two grain diameters  $d$  wide, one may question whether their model can be reliably applied to the typically much wider streams in nature ( $b/h \sim 10^0 \dots 10^3$ ). They attempted to account for their low  $b/h$  through an empirical correction of the bed shear stress. Yet their corrected data of the nondimensionalized bedload flux for spherical grains differ from older measurements for much wider and shallower channel flows by Ni and Capart (15) by a factor of 4 to 6 at the same nondimensionalized bed shear stress. However, such wide-shallow-channel flow experiments are also problematic, since, due to their shallowness (small  $h/d$ ), misidentifying the bed surface elevation by only a fraction of  $d$  can lead to a relatively large misestimation of the water weight responsible for shearing the bed. Ultimately, measurements of the nondimensionalized bedload flux for spherical grains carried out using distinct experimental facilities should more or less exhibit the same quantitative behavior if such channel geometry effects are appropriately accounted for. The fact that these two studies reported quantitatively so different measurements therefore indicates that at least one of them was inappropriately correcting for such effects, showcasing the need for a universal channel geometry correction method. Only then are we able to separate grain shape from channel geometry effects and test grain shape corrections with data from independent studies using distinct experimental facilities.

Here, we compile existing and new data of turbulent bedload transport of shape-controlled grains, obtained from experiments and grain-resolved (i.e., directly resolving fluid-particle interactions) and grain-unresolved numerical simulations based on various Computational Fluid Dynamics-Discrete Element Method (CFD-DEM) techniques, across channel flow widths and heights, grain shapes, bed slopes, and flow strengths. We reconcile channel geometry effects in these data through a universal sidewall correction, which we rigorously derive from an extension

of Kolmogórov’s theory of turbulence (16, 17), and a granular-physics-based definition to precisely determine the bed surface elevation (18). This channel geometry correction method is validated, among others, through a collapse of experimental and grain-resolved numerical bedload flux data for spherical grains on a unique behavior, whereas classical methods (11, 19–21) yield very large scatter. Furthermore, predictions from an existing physical bedload flux model (22), here straightforwardly generalized to account for grain shape variability, agree with the entire channel-geometry-corrected data compilation within a factor of 1.3, whereas Deal et al.’s (14) grain shape correction substantially increases the scatter in the data rather than reducing it, even when limited to the same kind of data (experiments and grain-resolved simulations) and the same range of the nondimensionalized bed shear stress as in their study.

## **Results**

### **Universal channel geometry correction method**

In order to isolate channel geometry effects on bedload flux, we begin with compiling existing experimental data sets for spherical grains, assuming that grain shape effects are negligible for them. The purpose is to reconcile them within a unifying framework. However, surprisingly, even though turbulent bedload transport has been studied for more than a century (23), flux measurements for spherical grains with a nearly uniform size distribution seem to be exceedingly scarce. After an extensive literature search, we have managed to find only a handful of data sets (14, 15, 24–27). Four of these were subsequently disregarded because of either partially crystallized beds and very large scatter (24, 25), or the presence of substantial suspended load in addition to bedload (26), or self-inconsistent data (27) (almost no bedload flux change with important variation of flow strength: increasing bed slope at constant flow depth). The only two remaining experimental data sets are those by Deal et al. (14) and Ni and Capart (15) discussed in the introduction. We therefore supplement the data compilation with additional data sets

from numerical simulations that couple the DEM for the particle phase with a CFD method for the fluid phase that resolves the sub-grain scale: two data sets based on Direct Numerical Simulations (DNS) (28, 29) for infinitely wide channels ( $b/h = \infty$ , i.e., periodic boundaries) and two data sets based on grain-resolved Large Eddy Simulations (LES) (12): one for  $b/h = \infty$  and one for a narrow-deep-channel configuration ( $b/h \approx 0.1$ ). Only such high-end methods, because they do not coarse-grain the particle phase and do not rely on empiricism for fluid-particle interactions, can be considered as similarly reliable as controlled experiments (30). Table 1 summarizes the data sets shown in this study, including those from experiments and grain-resolved simulations with non-spherical grains (13, 14, 31) and those from grain-unresolved CFD-DEM simulations (Refs. (22, 32, 33) and new simulations) discussed later.

The driving-flow strength in the experiments and grain-resolved simulations is quantified by the bed shear stress  $\tau_b$ , which is the fluid shear stress above the bedload transport layer extrapolated to the bed surface elevation within the fluid-particle mixture (Methods). In a wide channel (large  $b/d$ ), if it is also shallow (small  $h/d$ ) and/or if the bedload layer extends too close to the free surface of the liquid,  $\tau_b$  is sensitive to the precise definition of this elevation via the latter's influence on  $h$ . For such cases, we employ a granular-physics-based definition (18) (Methods). From an analogy to grain collisions with a rough base in inclined granular flows, it identifies the bed surface as the elevation at which the local production rate of the particle Reynolds stress is maximal. For other cases, in which spatial uncertainties of the bed surface elevation have only a marginal effect on  $\tau_b$ , we use the values of  $h$  reported in the respective studies. In addition,  $\tau_b$  must account for the presence of sidewalls. It is smaller than the sidewall-free bed shear stress  $\tau_{bo} \equiv (\langle \chi \rangle_z + \rho_f g \sin \alpha)h$  (Methods), where  $\rho_f$  is the fluid density,  $g$  the gravitational acceleration,  $\alpha$  the bed slope angle, and  $-\langle \chi \rangle_z$  the height-averaged streamwise pressure gradient ( $\chi = 0$  except for pressure-driven simulations). From the momentum balance

of the fluid-particle mixture, one can show (11) (Methods)

$$\tau_b = \frac{\tau_{bo}}{1 + \frac{2h}{b} f_w / f_b}, \quad (1)$$

where  $f_w \equiv \tau_w / (\rho_f U^2)$  and  $f_b \equiv \tau_b / (\rho_f U^2)$ , with  $U$  the bulk flow velocity and  $\tau_w$  the mixture sidewall shear stress, are the friction factors associated with the sidewalls and bed surface, respectively. The rougher these surfaces are, the larger is the rate at which the bulk flow energy density  $\rho_f U^2 / 2$  is frictionally dissipated, and the larger is the shear stress applied at them. The difficulty is now to relate the friction factor ratio  $f_w / f_b$  to the sidewall and bed surface roughnesses and the bulk flow properties. A classical, empirical approach employed in numerous studies is to assume  $f_w = f_b$ , in which case  $\tau_b = \tau_R \equiv (\langle \chi \rangle_z + \rho_f g \sin \alpha) R$ , where  $R \equiv hb / (b + 2h)$  is the hydraulic radius of the open channel (11). This prediction is consistent with measurements of flow velocity profiles in particle-free open channels consisting only of smooth sidewalls and bottom wall for a large range of width-to-depth ratios ( $b/h = 1.04-9.5$ ) (34). However, in sediment transport, where the bed surface is typically rougher than the smooth sidewalls ( $f_b > f_w$ ),  $\tau_R$  merely constitutes a lower bound of  $\tau_b$ . Another classical approach is the one by Einstein-Johnson (19-21) (Methods), in which  $f_w$  is determined from the empirical Karman-Prandtl law as the friction factor of a fully smooth channel and then  $f_b$  linked to  $f_w$  via an ad-hoc separation of the open channel into three parallel, non-interacting sidewall-free channels. However, this separation's only physical justification is its mathematically constructed consistency at the extreme limit  $f_b = f_w$ , where it rightfully predicts  $\tau_b = \tau_R$ . In contrast, the sidewall correction we derive here employs, for the Reynolds shear stress  $\tau_s$  at a given surface (the sidewalls or the bed), a relation based on Kolmogórov's theory of turbulence (16, 17):

$$\tau_s = -\rho_f \langle u'_{\parallel} u'_{\perp} \rangle = \kappa_{\tau} \rho_f U u_s, \quad (2)$$

where  $\langle \cdot \rangle$  denotes the Reynolds average. It states that the surface-parallel velocity fluctuations

$u'_{\parallel}$  are dominated by the largest turbulent eddies in the system, whose characteristic velocity is  $U$ , whereas the surface-normal velocity fluctuations  $u'_{\perp}$  emerge predominantly from the largest eddies that fit between neighboring roughness elements, which have a characteristic velocity  $u_s$ . This relation, which was previously used to derive Manning's (16) and Nikuradse's (17) empirical formulas from established physical principles for open channel and pipe flows, leads to  $f_w/f_b = u_w/u_b$ , where  $u_w$  and  $u_b$  are the values of  $u_s$  for the smooth sidewalls and rough bed surface, respectively. Importantly,  $u_w/u_b$  depends exclusively on approximately channel-geometry-independent (i.e., non-empirical) turbulence scaling coefficients (17) as the geometry-dependent coefficient  $\kappa_{\tau}$  in Eq. (2) cancels out (Methods):

$$f_w/f_b = 2.23\Re^{-1/4}(r/R)^{-1/3}. \quad (3)$$

Here  $r$  is the roughness size of the bed and  $\Re \equiv UR/\nu$  the bulk flow Reynolds number, with  $\nu$  the kinematic fluid viscosity. Since grains transported at elevations close to the bed surface tend to align their largest projected area parallel to the bed due to torque (13, 35), we choose the shortest grain axis  $c_g$  as the parameter setting  $r$  rather than the standard volume-equivalent sphere diameter  $d_0 \equiv \sqrt[3]{6V_p/\pi}$ , where  $V_p$  is the grain volume. Hence, assuming that about half the grain size is protruding into the flow for water-worked beds, we obtain  $r = c_g/2$  for sediment transport applications.

Once the bed shear stress  $\tau_b$  is determined using a given channel geometry correction method for the data from the experiments and grain-resolved simulations, we are able to fully characterize their hydrodynamic bedload transport conditions by dimensionless similarity parameters. We choose the particle-fluid density ratio  $s \equiv \rho_p/\rho_f$ , Galileo number  $Ga \equiv d\sqrt{s\tilde{g}_z d}/\nu$  (with  $\tilde{g}_z \equiv (1 - 1/s)g \cos \alpha$  the vertical submerged gravitational acceleration), Shields number  $\Theta \equiv \tau_b/(\rho_p\tilde{g}_z d)$ , dimensionless flow depth  $h^* \equiv h/d$ , and bed slope angle  $\alpha$  (Table 1). All data sets are well within the range of what is typically categorized as bedload transport



( $s \lesssim 10$  (22)), and most of them also satisfy  $s^{1/2}Ga \gtrsim 70$ , here termed “rough” conditions. In rough turbulent bedload, particle inertia dominate viscous fluid-particle interactions, and the nondimensionalized bedload flux  $Q_* \equiv Q/(\rho_p d \sqrt{s \tilde{g}_z d})$  is therefore expected to become essentially independent of  $s$  and  $Ga$  for sufficiently small  $\alpha$  (22, 23). We use this expectation as a tool to evaluate the different sidewall corrections outline above (Figs. 1A-1D). It can be seen that the data for rough turbulent bedload transport of spherical grains, indeed, collapse, within measurement uncertainty, on a universal  $Q_*(\Theta)$ -behavior for our method (Fig. 1D), but do not collapse at all when employing a classical method or left uncorrected (Figs. 1A-1C), or when using our sidewall correction but a different bed surface definition (NC18EXP\* in Fig. 1D). The only rough-turbulent-bedload data set that slightly deviates from the collapse in Fig. 1D is the data set Z22LESn in Table 1 (the data labeled as Z22LESn\* in Fig. 1). This is understandable given that the grid resolution of the grain-resolved LES simulations behind these data was limited to 15 times the Kolmogórov length scale (12), meaning that Kolmogórov’s theory of turbulence cannot be applied to them in a strict sense. However, an empirical reduction of this theory’s predicted scaling factor 2.23 in Eq. (3) by 20% leads to a data collapse (the data labeled as Z22LESn in Fig. 1). Henceforth, we apply this reduction to all data sets based on these simulations (Z22LESn, Z22LESw, and Z23LES) without further notice, though the data set Z22LESw is unaffected by this reduction due to  $b = \infty$ .

Figures 1E and 1F present further independent support for our sidewall correction. First, it predicts almost the same Shields numbers as those Deal et al. (14) empirically determined from fitting log-profiles to their flow velocity data, both for spherical and non-spherical grains (Fig. 1E). Second, it is also consistent with experimental data from particle-free flows in open channels ( $b/h = 2.94-7.79$ ) consisting of rough beds and smooth sidewalls (36–38) (Fig. 1F). As a side note, Fig. 1E also corroborates the previously questioned (39) reliability of Deal et al.’s (14) data and empirical methods. It means their strong quantitative difference to Ni and Capart’s

(15) reported spherical-grain data, discussed in the introduction, is found to be predominantly the consequence of the latter authors’ bed surface definition (NC18EXP\* in Fig. 1D). In fact, Fig. 2 shows that the resulting bed surface elevations are much below ours. It also highlights an important property of our method: the vertical profiles of the nondimensionalized local fluid shear stress  $\Theta_{xz}^f$  for various flow strengths exhibit a focal point at the bed surface elevation ( $z = 0$ ), with a focal value  $\Theta_{xz}^f(0) \approx 0.04$  close to the transport threshold Shields number  $\Theta_t$ . Pächt and Durán (18) presented theoretical arguments that, in the context of bedload transport, a physically meaningful bed surface definition should exhibit exactly this property among others. It therefore constitutes an independent piece of evidence supporting our bed surface definition and thus our channel geometry correction as a whole.

## Physical rough-bedload flux model across grain shapes, bed slopes, flow strengths and depths

**Bedload flux** Using a Reynolds-averaged Navier-Stokes (RANS)-based numerical model for the fluid phase coupled with the DEM for the motion of spherical grains, Pächt and Durán (22) simulated non-suspended sediment transport and derived a general transport rate expression holding for a large range of conditions, including turbulent bedload with  $s^{1/2}Ga \gtrsim 80$  and windblown sand:

$$Q_* = 2\kappa^{-1}\sqrt{\Theta_t}M_*(1 + c_M M_*). \quad (4)$$

Here  $\kappa = 0.41$  is the von Kármán constant,  $\Theta_t$  the transport threshold value of  $\Theta$ , and  $M_* \equiv M/(\rho_p d)$ , in which the transport load  $M$  denotes the average mass of “transported grains” (i.e., grains elevated above the bed surface) per unit area of the bed surface. Equivalently,  $M_*$  can be interpreted as a measure for the number  $N$  of transported grains above a bed area of size  $\sim d^2$ , that is, a particle activity (23) or a height-averaged particle concentration. The term  $c_M M_*$ , with  $c_M = 1.7$  a constant parameter determined from the simulations, encodes the rate of collisions

between transported grains ( $\propto M_*^2$ ) relative to that of grain-bed collisions ( $\propto M_*^1$ ). Equation (4) expresses the balance between global energy production due to drag (left-hand side) and energy dissipation due to grain contacts (right-hand side). In order to apply it to non-spherical grains, it is important to generalize  $d$  in a manner that retains  $M_* \sim N$ . Since grains transported at elevations close to the bed surface, where most transport takes place, tend to align their largest projected area  $A_p^{\max}$  parallel to the bed due to torque (13, 35), implying  $M \sim N \rho_p V_p / A_p^{\max}$ , this requirement begets  $d \equiv \frac{3}{2} V_p / A_p^{\max}$ . Introducing the longest ( $a_g$ ), intermediate ( $b_g$ ), and shortest ( $c_g$ ) axes of a grain, one can estimate  $V_p = \pi a_g b_g c_g / 6$  and  $A_p^{\max} = \pi a_g b_g / 4$ , leading to  $d = c_g$  (already used in Fig. 1E).

In steady, homogeneous sediment transport, the average vertical force on transported grains is dominated by gravity, buoyancy, and potentially fluid lift, since drag forces during the grains' upward motion tend to cancel those during their downward motion (42). When fluid lift is neglected, like in the simulations by Pahltz and Duran (18, 22), this implies that the particle pressure at the bed surface  $-\sigma_{zz}^p(0)$  is approximately equal to the submerged particle weight  $M\tilde{g}_z$ . The bed friction coefficient  $\mu_b \equiv -\sigma_{xz}^p(0)/\sigma_{zz}^p(0)$  then links  $M\tilde{g}_z$  to the surface particle shear stress  $\sigma_{xz}^p(0)$ . When further separating  $\sigma_{xz}^p(0)$  into gravity and drag contributions and assuming that particle drag on the fluid reduces the surface fluid shear stress  $\sigma_{xz}^f(0)$  to a value that is just sufficient to sustain transport, one obtains after some rearrangements Bagnold's (43) famous expression (18)

$$M_* = \frac{\Theta - \Theta_t}{\mu_b - \tan \alpha}, \quad (5)$$

which is a key ingredient of numerous bedload transport and windblown sand models in the literature, including the one by Pahltz and Duran (22). Historically, it has been assumed that  $\mu_b$  is equal to  $\mu_s$ , the tangent of the static angle of repose of the bulk bed material (43). However, RANS-DEM simulations of turbulent bedload transport of spherical grains suggest that, although constant,  $\mu_b$  is actually substantially larger than  $\mu_s$  ( $\mu_b \approx 0.7$  versus  $\mu_s \approx 0.4$ ) (18).

This observation can be understood as a bed surface strengthening effect. Bedload transport increases the bed surface’s ability to resist shear stress, since temporarily mobilized grains can settle again in more stable bed surface pockets (44). Whenever this happens, the bed surface becomes stronger relative to the bulk, i.e.,  $r_b \equiv \mu_b/\mu_s$  increases. This process continuous until a state is reached at which the pockets that emerge at the places where grains are mobilized are equivalent to the most stable pockets that transported grains can reach (44). Then,  $r_b$  has acquired its equilibrium value and will no longer increase. In viscous bedload, in which all pockets are reachable as a transported grain’s kinetic energy is typically much smaller than the potential energy wells of the bed surface,  $r_b \approx 3.4$  (45). However, in this study on turbulent bedload transport, where these two energy scales are of comparable size,  $r_b$  attains a smaller value as grains are too fast to probe the entire phase space of bed surface pockets (44). We use  $r_b = 1.8$  suggested by the simulations ( $1.8 \approx 0.7/0.4$ ) to calculate  $\mu_b$  from the measured  $\mu_s$ . In addition, we do not neglect lift forces as most previous studies. This straightforwardly leads to the following generalization of Eq. (5) (Methods), and thus of Pächtz and Durán’s (22) bedload flux model:

$$M_* = \mu_\dagger^{-1}(\Theta - \Theta_t), \quad \text{with} \quad \mu_\dagger \equiv r_b \mu_s \left[ \frac{1 + \left( \frac{s \tan \alpha}{s-1} + \overline{\chi^*} \right) \overline{f_L}/\overline{f_D}}{1 + r_b \mu_s \overline{f_L}/\overline{f_D}} \right] - \tan \alpha, \quad (6)$$

where  $\chi^* \equiv \chi/(\rho_p \tilde{g}_z)$ ,  $f_L$  and  $f_D$  are the lift and drag forces, respectively, per unit mass acting on transported grains, and the overbar denotes the particle-concentration-weighted height average. Equation (6) contains the single additional calibratable parameter  $\overline{f_L}/\overline{f_D}$ , whose influence is modulated by the control parameters  $s$ ,  $\alpha$ , and  $\overline{\chi^*}$ . It reduces to Eq. (5) if fluid lift is neglected. In real-world scenarios, one may expect  $\overline{f_L}/\overline{f_D}$  to be of order unity, as suggested by measurements of drag and lift forces acting on surface roughness elements, including grains in bed surface pockets (46, 47). We use  $\overline{f_L}/\overline{f_D} = 1.2$  because it optimizes the agreement between the final model and the entire data compilation.

**Transport threshold** The prefactor  $2\sqrt{\Theta_t}/\kappa$  in Eq. (4) resulted from interpreting  $\Theta_t$  as the smallest Shields number that permits a quasi-continuous hopping-rebound motion (saltation) of a test grain in a grain-motion-undisturbed logarithmic fluid velocity profile (22). In such a scenario, lift forces acting on the moving test grain are typically much smaller than drag forces (45) due to the formers’ rapid decrease with distance from the bed (47). Then, despite the distinct underlying physical picture, it can be shown for conditions with  $s^{1/4}Ga \gtrsim 200$  that  $\Theta_t$  in Eq. (4) obeys a scaling classically associated with the drag-induced mobilization of a grain resting in a bed surface pocket (45):

$$\Theta_t = c_t \left( r_b \mu_s - \frac{s \tan \alpha}{s - 1} \right) / C_D, \quad (7)$$

where  $c_t$  is a dimensionless parameter and  $C_D$  an effective drag coefficient parametrizing the streamwise drag force acting on grains, which depends on the settling velocity  $v_s$  and Corey shape factor  $S_f \equiv c_g / \sqrt{a_g b_g}$  (Methods). Since a typical threshold value for spherical grains is  $\Theta_t \approx 0.05$  (14), one expects  $c_t \approx 0.03$ . We use  $c_t = 0.032$  because it optimizes the agreement between the final model and the entire data compilation. On the other hand, when  $s^{1/4}Ga \lesssim 200$ , viscous-sublayer effects render the scaling of  $\Theta_t$  much more complicated (45). Therefore, we use Eq. (7) to determine  $\Theta_t$ , except for the few numerical conditions with  $s^{1/4}Ga < 200$  (BLRANSx in Table 1), for which we determine  $\Theta_t$  directly from the simulations, as described by Pantz and Duran (22). Note that the data sets J21DNS and KU17DNS in Table 1, which also satisfy  $s^{1/4}Ga < 200$ , are excluded from this discussion as they violate the precondition  $s^{1/2}Ga \gtrsim 80$  for Eq. (4).

**Model evaluation with entire data compilation** To evaluate our model, we require bedload flux data sets for shape-controlled grains, meaning they must provide the values of  $v_s$  and  $S_f$ , required to calculate  $C_D$ , and the value of  $\mu_s$ . The data sets D23EXPx satisfy this requirement (Table 1). Furthermore, in order to use the spherical-grain data set NC18EXP by Ni and Ca-

part (15), who did not report  $\mu_s$ , we acquired the same spheres from the same company and measured  $\mu_s$  using the funnel method (48) in the manner described by Deal et al. (14): by slowly pouring them onto an elevated disk bounded by a  $2d_0$ -high rim (Methods). Moreover, we scoured the literature and found two more usable experimental data sets for non-spherical grains: the bedload flux measurements for cylinders and lenses by Rebai et al. (31) (R22EXPx). For both grain shapes,  $v_s$  (49) and the grain dimensions (required for  $S_f$ ) have been reported, while  $\mu_s$  was measured using the funnel method in a box filled with water, which was sufficiently large to rule out potential box-sidewall friction effects (private correspondence with the authors). We confirmed with DEM simulations that different procedures of conducting the funnel method have only a small effect on  $\mu_s$  ( $< 5\%$ ) provided that a sufficiently large number of grains is used and that there is some means of preventing grains from rolling away (such as a rim or rough bed, see Methods).

Since our bedload flux model generalizes Bagnold’s (43) transport load expression, Eq. (5), to Eq. (6), involving the additional parameter  $\overline{f_L/f_D} = 1.2$ , we test it also for conditions to which Eq. (5) applies (i.e.,  $\overline{f_L/f_D} = 0$ ). For this purpose, we add data from grain-unresolved CFD-DEM simulations to the compilation, both from existing studies (22, 32, 33) and from new simulations, all of which were conducted using either of the numerical models described in Refs. (50–52) (Methods, Table 1). They differ from grain-resolved simulations in the fact that they do not resolve the flow around single grains, and they therefore incorporate empirical relations for the drag (Methods) and lift forces acting on particles, the latter of which are typically neglected (also here, i.e.,  $\overline{f_L/f_D} = 0$ ). They also allow us to perform gedankenexperiments in which  $C_D$  is treated as just another control parameter, since we can artificially modify  $C_D$  through changing the drag force parameters (Methods, LESCD and BLRANSCD in Table 1). Another purpose of adding these data is to confront our bedload flux model with transport conditions across a much larger range of the control parameters  $\Theta$ ,  $\alpha$ , and  $h^*$  than that spanned by the

experiments and grain-resolved simulations alone. Though some might consider it problematic to use arguably less realistic grain-unresolved simulations and enforce potentially non-relevant parameter values of  $\overline{f_L}/\overline{f_D}$  and  $C_D$ , we strongly believe that tests like this are warranted if one is truly interested in exploring the limitations and physical reasoning behind a given analytical model.

As a result of the wide range of control parameters and methods, the data of  $Q_*$  from the grain-unresolved simulations alone, and in extension from the entire data compilation, can vary by almost an order of magnitude at a given  $\Theta$  (Fig. 3). Nonetheless, the predictions from our bedload flux model deviate by less than a factor of 1.3 from almost all these data (Fig. 4). This does not only constitute a validation of our bedload flux model but also lends support to the reliability of the arguably somewhat artificial scenarios studied with the grain-unresolved simulations, since, if these were obeying different physics, one would not expect them to be captured by the same physical analytical model.

## Discussion

### The role of fluid lift in bedload transport

Our rough-bedload flux model combines the global energy balance, Eq. (4), after Pächtz and Durán (22), linking the bedload flux to the transport load, with Bagnold's (43) famous transport load expression, Eq. (6), generalized to account for a non-vanishing ratio  $\overline{f_L}/\overline{f_D}$  between the average lift and drag forces acting on transported grains. This is curious in so far as fluid lift is often assumed to be negligible in bulk bedload transport (14, 22, 45), mainly because once grains detach from the bed, the shear-induced lift force acting on them rapidly declines with elevation (47) and may even become negative (53, 54). In this regard, it is also interesting that  $\overline{f_L}/\overline{f_D}$  has no bearing on the transport threshold  $\Theta_t$  in Eq. (7). (We confirmed that including  $\overline{f_L}/\overline{f_D}$  in Eq. (7) in a fashion after Wiberg and Smith (55) results in failure of the overall model.)

The key difference between Eq. (6) and Eq. (7) is that the former is associated with liquid-like bulk bedload transport, in which many grains are in a rolling mode even for weak transport conditions (56), whereas the latter is obtained from a theoretical picture in which a single test grain continuously hops along the bed surface (i.e., a gas-like granular flow). This hints on the possibility that collectively rolling grains somehow cause the emergence of significant fluid lift in bulk bedload transport. For example, one might speculate that, in contrast to grains at rest, such grains are exposed to lifting lubrication forces, or that the rolling causes significant Magnus-like lift. However, exploring this or alternative possibilities requires further study in the future.

### **Test of Deal et al.’s (14) rough-bedload flux model with independent data**

We are only aware of a single alternative bedload flux model attempting to account for grain shape: the one by Deal et al. (14). These authors generalized  $d$  to the volume-equivalent sphere diameter  $d_0$ , as opposed to the shortest grain axis  $c_g$  in our model, and used the modified Shield number  $\Theta^{\text{D23}} \equiv \tau_b/(\rho_p \tilde{g}_z d_0)$  and modified nondimensionalized bedload flux  $Q_*^{\text{D23}} \equiv Q/(\rho_p d_0 \sqrt{(s-1)gd_0})$  to quantify the flow strength and transport rate, respectively. They proposed that bedload flux data corresponding to different grain shapes collapse onto a single curve  $Q_*^{\text{D23}} = f[(C^*/\mu^*)\Theta^{\text{D23}}]$ , where  $C^*$  is the sphere-normalized value of  $C_D d_0/c_g$  (Methods) and  $\mu^* \equiv (\mu_s - \tan \alpha)/(\mu_o - \tan \alpha)$ , with  $\mu_o = \tan 24^\circ$  the approximate value of  $\mu_s$  for spheres.

Deal et al. (14) validated their model with their bedload flux measurements for several grain shapes, but not with other experimental data from independent sources. Here, we test their model with the independent data sets from our data compilation, sidewall-corrected with our derived universal method (Fig. 5). We remind the reader that, when applied to Deal et al.’s (14) data sets, this correction yields almost the same bed shear stress  $\tau_b$  as their own empirical correction (Fig. 1E), while unifying spherical-grain data sets across experimental facilities (Fig. 1D).



So, any unfavorable outcome of this test is likely not attributable to the application of this new method. To be as fair as possible, we focus on those independent data sets obtained from experiments and grain-resolved simulations (Figs. 5A-5D) and use the entire data compilation only as a secondary addition to our arguments (Figs. 5E and 5F). It can be seen that Deal et al.'s (14) grain shape correction (Figs. 5B and 5D) much increases the scatter in the independent data when compared with the situation without correction (Figs. 5A and 5C), both for intense and weak transport conditions. In particular, the chosen range 0.05–0.25 of the (un)corrected Shields number in Figs. 5C and 5D is equivalent to the range of their own experiments (14), and the maximum scatter in Fig. 5D by more than a factor of 3 occurs well within this range, at  $(C^*/\mu^*)\Theta^{D23} \approx 0.14$ . It is caused by the data set R22EXPC in Table 1, for which  $C^*/\mu^* = 0.69$ , a more extreme value of  $C^*/\mu^*$  than in all their experiments ( $C^*/\mu^* = 0.84–1.05$ ) (14).

We believe that this poor performance chiefly results from their incorporation of  $C^*$  in their grain shape correction of the Shields number. In fact, it was shown that models that express bedload flux as a function of the excess bed shear stress are inherently linked to Bagnold's (43) (later confirmed) assumption of a constant friction coefficient at the bed surface (18), which is  $\mu_s$  in the case of their model and  $\mu_b = r_b\mu_s$  in the case of ours. In equilibrium, this constant friction coefficient is equal to the ratio between the average streamwise and normal-bed forces acting on transported grains, rendering the average drag force per unit mass  $\overline{f_D}$  insensitive to the details of the flow. In consequence, increments of  $C^*$  (or  $C_D$  in our model) tend to be compensated by decrements of the average fluid-particle velocity difference, keeping  $\overline{f_D}$  and therefore the effective transport-driving shear stress constant. Note that this reasoning is corroborated by the fact that the yellow symbols in Figs. 5E and 5F, corresponding to conditions with artificially strongly elevated values of  $C^*$  or  $C_D$  (LESCD and BLRANSCD in Table 1), shift far away from the rest of the data after employing Deal et al.'s (14) grain shape correction. In contrast, they are captured by our bedload flux model (Fig. 4D) because it does not modify the Shields

number  $\Theta$  by a drag-dependent correction.

## Bedload flux variability

Given the large diversity of conditions and experimental and numerical methods (Table 1), the level of agreement between our model and the channel-geometry-corrected data in Fig. 4 is remarkable. It suggests that, with the here employed universal sidewall correction and bed surface definition, and our physical model to predict the flux of rough bedload transport (applicable if  $s^{1/2}Ga \gtrsim 80$ , satisfied for most conditions in nature), bedload variability is largely diminished, at least for the idealized case considered here (steady flows over flat beds at short timescales). This is a prerequisite for discerning different sources of variability in the more complex situations typically encountered in nature.

## Methods

### Streamwise momentum balances and bed shear stress

**Streamwise fluid momentum balance** For a statistically steady ( $\partial_t = 0$ ) and streamwise uniform ( $\partial_x = 0$ ) fluid-particle mixture flow in an open channel with sidewalls, the streamwise fluid momentum balance, averaged over time  $t$  and the flow direction  $x$ , reads (57)

$$\rho_f \partial_y \tilde{\epsilon} \tilde{u}_y \tilde{u}_x + \rho_f \partial_z \tilde{\epsilon} \tilde{u}_z \tilde{u}_x = \partial_y \tilde{\tau}_{xy}^f + \partial_z \tilde{\tau}_{xz}^f + \tilde{\chi} + \rho_f \tilde{\epsilon} g \sin \alpha - \rho_p \tilde{\phi} \tilde{f}_x^{f \rightarrow p}, \quad (8)$$

where  $\rho_p$  and  $\rho_f$ ,  $g$ ,  $\alpha$ ,  $\tilde{\epsilon}$  and  $\tilde{\phi} = 1 - \tilde{\epsilon}$ ,  $\tilde{\mathbf{u}}$ ,  $\tilde{\tau}_{ij}^f$ , and  $\tilde{\mathbf{f}}^{f \rightarrow p}$  are the particle and fluid density, gravitational acceleration, bed slope angle, average fluid and particle volume fractions, fluid velocity, fluid shear stress tensor, and fluid-particle interaction force per unit mass, respectively, and  $-\tilde{\chi}$  is a streamwise pressure gradient ( $\tilde{\chi} = 0$  except for the pressure-driven bedload transport simulations). Further averaging over the cross-channel direction  $y \in (-b/2, b/2)$  (denoted

as  $\langle \cdot \rangle_y$ , with  $y = 0$  the channel center and  $b$  the channel width, then yields

$$d_z(\tau_{xz}^f - \rho_f \epsilon u_z u_x) = 2(\tilde{\tau}_w^f - \rho_f \tilde{\epsilon}_w \tilde{u}_{w\perp} \tilde{u}_{w\parallel})/b - \chi - \rho_f \epsilon g \sin \alpha + \rho_p \phi f_x^{f \rightarrow p}, \quad (9)$$

where  $\tilde{\tau}_w^f \equiv \mp \tilde{\tau}_{xy}^f(\pm b/2)$ ,  $\tilde{\epsilon}_w \equiv \tilde{\epsilon}(\pm b/2)$ ,  $\tilde{u}_{w\perp} \equiv \mp \tilde{u}_y(\pm b/2)$  and  $\tilde{u}_{w\parallel} \equiv \tilde{u}_x(\pm b/2)$  are the fluid shear stress, average fluid volume fraction, average normal and tangential fluid velocities, respectively, at the sidewalls, and quantities without a tilde are analogous to those with a tilde but with respect to the overall average over  $t$ ,  $x$ , and  $y$ , except for stress the fluid shear stress  $\tau_{xz}^f$ . The latter also consists of an additional Reynolds stress contribution from the  $y$ -averaging:

$$\tau_{xz}^f \equiv \langle \tilde{\tau}_{xz}^f \rangle_y - \rho_f \epsilon \langle \tilde{u}'_x \tilde{u}'_z \rangle_y^f, \quad (10)$$

where  $\tilde{\mathbf{u}}' \equiv \tilde{\mathbf{u}} - \mathbf{u}$  is the fluctuation fluid velocity with respect to the fluid-phase-weighted cross-channel average, defined as  $\langle \cdot \rangle_y^f \equiv \langle \tilde{\epsilon} \cdot \rangle_y / \epsilon$ . Finally, integration of Eq. (9) from the bed surface elevation  $z = 0$  to the flow depth elevation  $z = h$ , exploiting that  $\tau_{xz}^f(h)$  and the boundary-averaged normal fluid fluxes  $\epsilon(0)u_z(0)$  and  $\langle \tilde{\epsilon}_w \tilde{u}_{w\perp} \rangle_z$  approximately vanish, with  $\langle \cdot \rangle_z \equiv \frac{1}{h} \int_0^h \cdot dz$  the height average, yields

$$\tau_{xz}^f(0) = (\langle \chi \rangle_z + \rho_f g \sin \alpha) h - 2h\tau_w^f/b - M \left( s^{-1} g \sin \alpha + \bar{f}_x^{f \rightarrow p} \right), \quad (11)$$

where  $M \equiv \rho_p \int_0^h \phi dz$  is the transport load,  $s \equiv \rho_p / \rho_f$  the particle-fluid density ratio,  $\bar{\cdot} \equiv \langle \phi \cdot \rangle_z / \langle \phi \rangle_z$  the  $\phi$ -weighted height average, and  $\tau_w^f$  the average sidewall fluid shear stress, given by

$$\tau_w^f \equiv \langle \tilde{\tau}_w^f \rangle_z - \rho_f \langle \tilde{\epsilon}_w \rangle_z \langle \tilde{u}'_{w\perp} \tilde{u}'_{w\parallel} \rangle_z^f, \quad (12)$$

with  $\tilde{u}'_{w\perp, \parallel} \equiv \tilde{u}_{w\perp, \parallel} - \langle \tilde{u}_{w\perp, \parallel} \rangle_z^f$  the fluctuation sidewall fluid velocity with respect to the fluid-phase-weighted height average at the sidewalls, defined as  $\langle \cdot \rangle_z^f \equiv \langle \tilde{\epsilon}_w \cdot \rangle_z / \langle \tilde{\epsilon}_w \rangle_z$ .

**Streamwise particle momentum balance** Analogous to Eq. (11), the height-integrated overall average streamwise particle momentum balance reads (57)

$$\sigma_{xz}^p(0) = -2h\tau_w^p/b + M \left( g \sin \alpha + \bar{f}_x^{f \rightarrow p} \right), \quad (13)$$

where  $\tau_w^p$  the average sidewall particle shear stress and  $\sigma_{ij}^p$  the particle stress tensor. They consist of contributions from the particle fluctuation motion, local contact forces, and the grains' rotational motion (for precise definitions, see Ref. (57)).

**Streamwise mixture momentum balance and bed shear stress definition** Summing Eqs. (11) and (13) yields the streamwise mixture momentum balance:

$$\tau_{xz}^f(0) + \sigma_{xz}^p(0) = \tau_b + M\tilde{g}_z \tan \alpha, \quad (14)$$

where  $\tilde{g}_z \equiv (1 - 1/s)g \cos \alpha$  is the vertical submerged gravitational acceleration and  $\tau_b$  the bed shear stress, defined as

$$\tau_b \equiv (\langle \chi \rangle_z + \rho_f g \sin \alpha) h - \frac{2h}{b} \tau_w \equiv \tau_{bo} - \frac{2h}{b} \tau_w, \quad (15)$$

with  $\tau_w \equiv \tau_w^f + \tau_w^p$  the mixture sidewall shear stress. Equation (15) can be rearranged to yield Eq. (1).

**Streamwise fluid momentum balance for flow in an inner turbulent boundary layer** The model of Ref. (50) considers a flow in an inner turbulent boundary layer of infinite height (no sidewalls). To be consistent with Eq. (14), we slightly modified the streamwise momentum balance in Ref. (50) to

$$d_z \tau_{xz}^f = \rho_f \phi g \sin \alpha + \rho_p \phi f_x^{f \rightarrow p}, \quad \text{with} \quad \tau_{xz}^f(\infty) = \tau_b, \quad (16)$$

before conducting simulations.

**Relationship between bed shear stress and logarithmic fluid velocity profile** For turbulent bedload transport in open channels, there is a limited region in the clear-water flow above the

bedload layer where the fluid velocity profile approximately satisfies the logarithmic law of the wall (14, 28, 58):

$$u_x \simeq \frac{u_\tau^{\log}}{\kappa} \ln \frac{z}{z_o}, \quad (17)$$

with  $\kappa = 0.41$  the von Kármán constant,  $z_o$  the hydrodynamic roughness, and  $u_\tau^{\log} \equiv \sqrt{\tau_{\log}/\rho_f}$  the friction velocity. In DNS-DEM simulations of bedload transport, the associated shear stress  $\tau_{\log}$  is equivalent to the bed shear stress defined by Eq. (15) (28, 58):

$$\tau_{\log} \simeq \tau_b. \quad (18)$$

Although these simulations were conducted under zero-slope conditions in the absence of sidewalls, we assume that Eq. (18) holds true also under more general circumstances.

## Universal sidewall correction

Equation (18) indicates that  $\tau_b$  can be understood as the value of  $\tau_{xz}^f(z)$  extrapolated from the particle-free region above the transport layer to the bed surface elevation  $z = 0$ . In the same spirit, we interpret  $\tau_w$  as the value of  $\frac{1}{h-z} \int_z^h [\tilde{\tau}_w^f(z') - \rho_f \tilde{\epsilon}_w \tilde{u}'_{w\perp} \tilde{u}'_{w\parallel}] dz'$  (cf. Eq. (12)), where the prime refers to fluctuations with respect to the fluid phase average over heights between  $z$  and  $h$ , extrapolated from the particle-free region to  $z = 0$ . Based on these interpretations, we assume that the stress ratio  $\tau_w/\tau_b$ , which is equivalent to the friction factor ratio  $f_w/f_b$  in Eq. (1), can be modeled as if the flow above the bed was devoid of grains. Using Kolmogórov's theory of turbulence, it can be written as (16, 17)

$$\tau_w/\tau_b = f_w/f_b = u_w/u_b, \quad (19)$$

where  $u_b$  and  $u_w$  are the characteristic values of the largest normal velocities that turbulent eddies can generate near the sidewalls and bed surface, respectively. These are eddies of sizes controlled by the roughness size  $r$  of the rough bed and by the thickness  $5(\kappa_\epsilon \kappa_u^3/2)^{-1/4} R\Re^{-3/4}$

of the viscous sublayer adjacent to the smooth sidewalls, respectively. Here  $R \equiv hb/(b+2h)$  is the hydraulic radius,  $\Re \equiv UR/\nu$  the Reynolds number, with  $U$  the bulk fluid velocity and  $\nu$  the kinematic fluid viscosity,  $\kappa_\epsilon = 5/4$  a constant that follows from Kolmogórov's four-fifths law, and  $\kappa_u \equiv u_R/U$  a parameter that relates the characteristic velocity  $u_R$  of the largest eddies to  $U$ . It is found to be highly insensitive to flow geometry, with  $\kappa_u = 0.036 \pm 0.005$  measured in pipe flow (59) and  $\kappa_u = 0.033$  in the atmospheric boundary layer (60). With these parameters,  $u_w/u_b$  can be calculated by Eq. (2) of Ref. (17) as

$$\frac{u_w}{u_b} = \frac{[5(\kappa_\epsilon \kappa_u^3/2)^{-1/4} R \Re^{-3/4}]^{1/3} \sqrt{(\beta/5)^{2/3} \Gamma_{-2/3}(\beta/5)}}{r^{1/3}} = c_{wb} \Re^{-1/4} (r/R)^{-1/3}, \quad (20)$$

where  $\beta = [3\Gamma(4/3)]^{3/4}$  is the characteristic constant of the exponential decay of the velocity spectrum of turbulent flow, and  $c_{wb} \simeq 2.23$  is the scaling coefficient resulting from evaluating the expression in the middle. Since it depends only on  $\kappa_\epsilon$ ,  $\kappa_u$ , and  $\beta$ , it is an approximately channel-geometry-independent, that is, non-empirical parameter. Using Eq. (19),  $u_w/u_b$  is equivalent to  $f_w/f_b$ , which inserted into Eq. (1) yields the sidewall-corrected bed shear stress  $\tau_b$ .

In order to use Eq. (20), one needs to know  $U$ , which we calculate from the measured fluid discharge  $Q_f$  as (31)

$$U = \frac{Q_f}{b \left( h - \int_0^h \phi dz \right)}. \quad (21)$$

Note that, except for intense sediment transport, the term  $\int_0^h \phi dz$  has only a marginal effect on  $\tau_b$ . Hence, for the data sets D23EXPx (14) (Table 1), for which concentration profile data is not available, we calculate  $U$  as  $U \simeq Q_f/(bh)$ .

## Einstein-Johnson's sidewall correction

The empirical sidewall correction by Einstein and Johnson (19, 20) calculates the friction factor ratio  $f_w/f_b$  in Eq. (1) as (21)

$$\begin{aligned} f_w/f_b &= R_w/R_b, \quad \text{with} \quad R_b = (1 - 2R_w/b), \quad R_w = f^{-1}R[6 \log_{10} [W(x)/x]]^{-2}, \\ f &= 8U^{-2}gR \sin \alpha, \quad x = [9\Re/(100f)]^{1/3}, \end{aligned} \quad (22)$$

where  $W(x)$  denotes the principal branch of the Lambert  $W$  function.

## Maximum fluid shear stress

An alternative measure for the driving shear stress is the maximum fluid shear stress (51):

$$\tau_{cl} \equiv \max \tau_{xz}^f(z). \quad (23)$$

We use this definition in our grain-unresolved CFD-DEM simulations, since the raw data required to determine the bed surface elevation  $z = 0$ , and thus  $h$  and  $\tau_b$ , could no longer be located for the data sets M18RANS (32) and M19RANSx (33) (Table 1). In contrast to  $\tau_b$ ,  $\tau_{cl}$  is not associated with the particle-fluid mixture but can be interpreted as an effective clear-water fluid shear stress acting on the top of the bedload layer (32). Using  $\tau_b \propto h$  (Eq. (15)), it therefore defines an effective clear-flow depth as

$$h_{cl} \equiv h\tau_{cl}/\tau_b \quad (24)$$

and subsequently an effective bedload layer thickness above the bed surface as

$$h_p \equiv h - h_{cl}. \quad (25)$$

The latter is linked to the transport load  $M$  via

$$M = \rho_p h_p \underline{\phi}, \quad (26)$$

with  $\bar{\cdot} \equiv \frac{1}{h_p} \int_0^h \cdot dz \approx \frac{1}{h_p} \int_0^{h_p} \cdot dz$  the approximate average of a particle quantity over the bedload layer thickness. Combining the above relations yields an expression linking the Shields numbers  $\Theta \equiv \tau_b/(\rho_p \tilde{g}_z d)$  and  $\Theta_* \equiv \tau_{cl}/(\rho_p \tilde{g}_z d)$  with one another:

$$\Theta = \Theta_* + \frac{\Theta_*}{\underline{\phi} h_{cl}^*} M_*, \quad (27)$$

where  $h_{cl}^* \equiv h_{cl}/d$  and  $M_* \equiv M/(\rho_p d)$  are the dimensionless clear-flow depth and transport load, respectively, with  $d$  the generalized grain diameter. The parameter  $\underline{\phi}$  in Eq. (27) is determined directly from the numerical data in the Methods section entitled ‘Estimation of bed shear stress and its uncertainty’. Note that, for our inner turbulent boundary layer simulations,  $h_{cl}^* = \infty$  and therefore  $\Theta = \Theta_*$ .

## Transport load expressions

To derive simple expressions for the dimensionless transport load  $M_*$ , we henceforth neglect the contributions of particle-sidewall friction in the streamwise ( $\tau_w^p$  in Eq. (13)) and vertical particle momentum balances. Analogous to the former, the latter balance reads

$$d_z \sigma_{zz}^p = \rho_p \phi g \cos \alpha - \rho_p \phi f_z^{f \rightarrow p}. \quad (28)$$

In both balance equations, we separate fluid-particle interactions into buoyancy and non-buoyancy contributions. The latter are identified as the drag ( $f_D$ ) and lift ( $f_L$ ) forces per unit mass for the streamwise and vertical directions, respectively:

$$f_D \equiv f_x^{f \rightarrow p} - \chi/\rho_p, \quad (29)$$

$$f_L \equiv f_z^{f \rightarrow p} - s^{-1} g \cos \alpha, \quad (30)$$

where Eq. (29) takes into account that buoyancy forces arise from instantaneous stresses, but not Reynolds stresses, and that the contribution of the instantaneous viscous shear stress to



the streamwise buoyancy force can be neglected in turbulent bedload transport (32). Using Eqs. (29) and (30), Eq. (13) and the integrated Eq. (28), respectively, become

$$\sigma_{xz}^p(0) = M \left( g \sin \alpha + \bar{\chi}/\rho_p + \bar{f}_D \right), \quad (31)$$

$$\sigma_{zz}^p(0) = -M \left( \tilde{g}_z - \bar{f}_L \right). \quad (32)$$

It follows that the bed friction coefficient, defined as  $\mu_b \equiv -\sigma_{xz}^p(0)/\sigma_{zz}^p(0)$ , constrains the average forces acting on transported grains:

$$\mu_b = \frac{g \sin \alpha + \bar{\chi}/\rho_p + \bar{f}_D}{\tilde{g}_z - \bar{f}_L}. \quad (33)$$

This equation can be transformed into

$$\bar{f}_D = \frac{\mu_b \tilde{g}_z - g \sin \alpha - \bar{\chi}/\rho_p}{1 + \mu_b \bar{f}_L/\bar{f}_D}. \quad (34)$$

Furthermore, combining Eq. (31) with Eq. (14) and nondimensionalization leads to

$$\Theta - \Theta_{xz}^f(0) = M_* \left[ \left( \frac{s \tan \alpha}{s-1} + \bar{\chi}^* + \frac{\bar{f}_D}{\tilde{g}_z} \right) - \tan \alpha \right], \quad (35)$$

with  $\bar{\chi}^* \equiv \bar{\chi}/(\rho_p \tilde{g}_z)$  and  $\Theta_{xz}^f \equiv \tau_{xz}^f/(\rho_p \tilde{g}_z d)$ . Finally, insertion of Eq. (34), optionally using Eq. (27), yields

$$M_* = \mu_{\dagger}^{-1} [\Theta - \Theta_{xz}^f(0)], \quad (36)$$

$$M_* = \left( \mu_{\dagger} - \frac{\Theta_*}{\phi h_{cl}^*} \right)^{-1} [\Theta_* - \Theta_{xz}^f(0)], \quad (37)$$

$$\text{with } \mu_{\dagger} \equiv \mu_b \left[ \frac{1 + \left( \frac{s \tan \alpha}{s-1} + \bar{\chi}^* \right) \bar{f}_L/\bar{f}_D}{1 + \mu_b \bar{f}_L/\bar{f}_D} \right] - \tan \alpha.$$

**Exploiting bed surface properties** Up to this point, the only approximation involved in the derivation of Eqs. (36) and (37) is the disregard of particle-sidewall friction. Now, we apply the following additional simplification to obtain Eq. (6):

$$\Theta - \Theta_{xz}^f(0) \approx \Theta - \Theta_t. \quad (38)$$

Equation (38) could be interpreted as a consequence of  $\Theta_{xz}^f(0) \approx \Theta_t$ , which is Bagnold's hypothesis (43) that the near-surface flow velocity in bedload transport reduces to the threshold value that is barely sufficient to sustain grain motion. However, in actuality  $\Theta_{xz}^f(0) \approx \Theta_t$  is not a necessary requirement for Eq. (38) to hold (for details, see Ref. (18)). Moreover, for Eq. (38) to be justified, the bed surface elevation  $z = 0$  must be defined appropriately (see below and Fig. 2).

### Definition of bed surface elevation

Pächtz and Durán (18) defined the bed surface as the elevation at which the local production rate  $-\sigma_{zz}^p \dot{\gamma}$ , with  $\dot{\gamma} \equiv d_z v_x$  the particle shear rate, of the cross-correlation particle fluctuation energy  $-\rho_p \phi v_x v_z$  (the particle Reynolds stress) is maximal. Their physical reasoning was based on an analogy to grain collisions with a rough base in inclined granular flows. They showed that, for data from DEM-RANS simulations of non-suspended sediment transport across a large range of bedload and windblown sand conditions, bed surface elevations defined in this manner satisfy  $\mu_b \approx \text{const}$  and, for  $\Theta \lesssim 0.4$ ,  $\Theta_{xz}^f(0) \approx \Theta_t$ , consistent with the assumption Eq. (38). Since their simulations did not consider lift forces ( $f_L \equiv 0$ ), it follows from Eqs. (28) and (30) that their definition was essentially equivalent to

$$\max(\dot{\gamma} \Sigma \phi) = [\dot{\gamma} \Sigma \phi]_{z=0}, \quad (39)$$

with  $\Sigma \phi(z) \equiv \int_z^h \phi(z') dz'$ .

### Estimation of bed shear stress and its uncertainty

We apply Eq. (39) to determine the bed surface elevation  $z = 0$ , and from it the flow depth  $h$ , for the experimental wide-channel data sets NC18EXP and R22EXPx (Table 1), assuming that the reported time-averaged, local particle concentration and velocity profiles are proxies

for the respective overall averages over  $t$ ,  $x$ , and  $y$ . Regarding velocity profiles, this standard assumption (11) is supported by measurements (38).

**NC18EXP** For this highly-resolved data set, the profiles of  $\dot{\gamma}\Sigma\phi$  exhibit several local maximums due to layering (Fig. 6A). We choose the top-most local maximum at the bed surface elevation  $z = 0$  because the profiles  $\Theta_{xz}^f(z)$  exhibit a focal point there, with  $\Theta_{xz}^f(0) \approx \Theta_t$  (Fig. 2), consistent with the theoretical expectation (18). It occurs  $\Delta z = 31.75 \pm 0.5$  mm above the channel bottom for all flow conditions. The upper and lower bounds  $\Delta z = 32.25$  mm and  $\Delta z = 31.25$  mm then yield corresponding lower ( $h_{\min}$ ) and upper ( $h_{\max}$ ) bounds, respectively, of  $h$  for a given flow condition, with corresponding bed shear stress estimates  $\tilde{\tau}_b(h_{\max})$  and  $\tilde{\tau}_b(h_{\min})$ , respectively, obtained from Eqs. (1) and (3). Hence, we estimate  $\tau_b$  and its uncertainty as

$$\tau_b = \frac{1}{2} [\tilde{\tau}_b(h_{\max}) + \tilde{\tau}_b(h_{\min})] \pm \frac{1}{2} [\tilde{\tau}_b(h_{\max}) - \tilde{\tau}_b(h_{\min})]. \quad (40)$$

**R22EXPx** Two data sets are reported: one for cylindrical grains (R22EXPC) and one for grains with a lens shape (R22EXPI). Since the authors' experimental methods did not resolve  $v_x(z)$  inside the sediment bed (31) and due to an insufficient data resolution for reliably calculating velocity gradients, the vertical profiles of  $\dot{\gamma}\Sigma\phi$  are of a rather poor quality near the bed (Figs. 6B and 6C), with some of the cylinder data not even exhibiting a pronounced maximum of  $\dot{\gamma}\Sigma\phi$ . For R22EXPI, we determine  $h$  from the most pronounced maximum and calculate the ratio  $R_h \equiv h/h^{\text{R22}}$ , where  $h^{\text{R22}}$  is the reported flow depth value. It was measured as the depth over the mean of (i) the elevation at which the linear extrapolation of  $v_x(z)$  vanishes and (ii) the interpolated elevation at which the particle volume fraction  $\phi = 0.6$  (31). Since this method requires neither particle velocity data inside the sediment bed nor calculating particle velocity gradients,  $h^{\text{R22}}$  is more much precisely determinable than  $h$ . The value of  $R_h$  varies, indeed, little with flow conditions for R22EXPI, between about  $\min(R_h) = 0.91$  and

$\max(R_h) = 1.02$ . Assuming that, under hypothetically experimentally ideal conditions,  $R_h$  does not depend on the flow condition, we use it to obtain  $\tau_b$  and its uncertainty range from the estimate  $\tilde{\tau}_b^{\text{R22}} = \tilde{\tau}_b(h^{\text{R22}})$  for both R22EXPI and R22EXPC as follows:

$$\tau_b = \frac{1}{2} [\max(R_h) + \min(R_h)] \tilde{\tau}_b^{\text{R22}} \pm \frac{1}{2} [\max(R_h) - \min(R_h)] \tilde{\tau}_b^{\text{R22}}. \quad (41)$$

**Z22LESw** The values of  $h^*$  reported for this data set are based on Eq. (39) (12). We therefore use the reported values of  $h^*$  and  $\Theta$ , assuming that the uncertainty of  $\Theta$  is very small (smaller than the respective symbols in the plots).

**D23EXPx, Z22LESn, and Z23LES** For these data sets, we use the reported values of  $h$  as its effect on  $\tau_b$  is very small because of very small width-to-depth ratios ( $b/h \approx 0.1$ ) and because  $h$  was much larger than the bedload layer thickness (12–14). For the numerical data sets Z22LESn and Z23LES, we therefore conclude that the uncertainty of  $\tau_b$  is very small (smaller than the respective symbols in the plots). For the experimental data sets D23EXPx, the main source of uncertainty comes from the determination of the bed slope angle  $\alpha$ . We propagate its reported uncertainty to estimate the uncertainty of  $\tau_b$ .

**J21DNS and KU17DNS** As we do not have access to the raw data of these data sets, and since  $h$  was much larger than the bedload thickness (28, 29), we use the reported values of  $h^*$  and  $\Theta$ , assuming that the uncertainty of  $\Theta$  is very small (smaller than the respective symbols in the plots).

**M18RANS, M19RANSx, LESx** For these data sets, we determine  $h^*$  and subsequently  $\Theta$  from  $\Theta_*$  and  $h_{c1}^*$ , both of which can be determined with negligible uncertainty. In order to determine  $\Theta$  using Eq. (27), one needs to know the value of  $\underline{\phi}$ . To this end, we calculate  $M_*$  from the  $Q_*$ -data via Eq. (4), using the predicted value of  $\Theta_t$  from Eq. (7), and subsequently  $\underline{\phi}$

from  $M_*$ ,  $\Theta_*$ , and  $h_{cl}^*$  via Eq. (27). Figure 7 shows the resulting behavior of  $\underline{\phi}$  as a function of  $J \equiv \Theta_*/[h_{cl}^*(r_b\mu_s - \tan\alpha)]$ . We are interested in the value of  $\underline{\phi}$  in the limit of large  $J$ , since the ratio  $\Theta/\Theta_*$  deviates the more from unity the larger  $J$  (inset of Fig. 7). It can be seen that, in this limit,  $\underline{\phi} \approx 0.25$ . This value is reasonable as it is about half of  $\phi(0)$  for intense transport conditions (18).

Although we use the  $M_*$ -values calculated from the  $Q_*$ -data for the determination of  $\underline{\phi}$ , we do not do so when estimating  $\Theta$ , in order to avoid an implicit dependence of  $\Theta$  on  $Q_*$ . Instead, we obtain  $\Theta$  from the values of  $M_*$  predicted by Eq. (37) with  $\underline{\phi} = 0.25$ . The uncertainty of  $\Theta$  in Figs. 4B and 4B, and subsequently that of  $\Theta^{D23}$  in Figs. 5E and 5F, then corresponds to the propagated uncertainty of  $\mu_s$  in the calculation of  $\Theta$  via Eqs. (27) and (37).

**BLRANSx** For these data sets,  $h^* = \infty$  by construction and  $\Theta$  is a preset parameter (no uncertainty).

## Drag coefficient

**Drag coefficient in experiments and grain-resolved CFD-DEM simulations** The drag coefficient  $C_D$  in Eq. (7) parametrizes the effective streamwise drag force acting on grains. It is smaller than that for settling grains,  $C_{D\text{Settle}} = 4(s-1)gd/(3v_s^2)$  (14), where  $v_s$  is the terminal grain settling velocity, due to the smaller projected area exposed to the flow. Assuming again that transported grains tend to align their largest projected area  $A_p^{\text{max}} = \pi a_g b_g/4$  parallel to the bed, with  $a_g$  and  $b_g$  the long and intermediate grain axes, the effective projected area  $A_p^{\text{eff}}$  in the streamwise direction is estimated as the geometric mean of the remaining two projected areas  $\pi a_g c_g/4$  and  $\pi b_g c_g/4$ :  $A_p^{\text{eff}} = \pi \sqrt{a_g b_g} c_g/4$ , implying  $A_p^{\text{eff}}/A_p^{\text{max}} = c_g/\sqrt{a_g b_g} \equiv S_f$ , which is the Corey shape factor. Hence, in spite of a different physical reasoning, we arrive at the same

expression as Deal et al. (14):  $C_D = S_f C_{D\text{Settle}}$  or

$$C_D = 4S_f(s-1)gd/(3v_s^2). \quad (42)$$

However, note that the values of  $C_D$  for non-spherical grains differ from those in Deal et al. (14) due to a different definition of  $d$ .

**Drag coefficient in grain-unresolved CFD-DEM simulations** The numerical CFD-DEM models that do not resolve the sub-grain scale rely on semiempirical relations for fluid-particle interactions. They consider buoyancy and drag forces on spheres or composite grains consisting of non-overlapping component spheres, but neglect lift forces. Following Ref. (61), the drag force is modeled as the total force on all component spheres:

$$\mathbf{F}_D = \sum_i \frac{1}{8} \rho_f \pi d_i^2 \left[ \left( \frac{\Re_c \nu}{d_i \epsilon^{p_1}} \right)^{1/m} + \left( \frac{C_D^\infty |\mathbf{u}_r|}{\epsilon^{p_2}} \right)^{1/m} \right]^m \mathbf{u}_r, \quad (43)$$

where  $d_i$  is the diameter of the  $i$ -th component sphere,  $\mathbf{u}_r$  the fluid-particle velocity difference, and  $\Re_c$ ,  $C_D^\infty$ ,  $m$ ,  $p_1$ , and  $p_2$  are empirical parameters (Table 2). Dividing Eq. (43) by the grain weight  $\frac{\pi}{6} \sum_i d_i^3$  leads to an expression for the ratio between the drag acceleration  $\mathbf{a}_D$  and submerged gravitational acceleration  $\tilde{g} \equiv (1 - 1/s)g$  in terms of nondimensionalized quantities:

$$\frac{\mathbf{a}_D}{\tilde{g}} = \frac{3}{4} \left[ \left( \frac{\Re_c}{\widetilde{Ga} \epsilon^{p_1}} \right)^{1/m} + \left( \frac{C_D^\infty |\tilde{\mathbf{u}}_r|}{\epsilon^{p_2}} \right)^{1/m} \right]^m \tilde{\mathbf{u}}_r, \quad (44)$$

where  $\tilde{\mathbf{u}}_r \equiv \mathbf{u}_r / \sqrt{s\tilde{g}d}$ , with  $d \equiv \frac{3}{2} V_p / A_p^{\max} = \sum_i d_i^3 / \sum_i d_i^2$ , is the nondimensionalized fluid-particle velocity difference and

$$\widetilde{Ga} \equiv \frac{\sqrt{(\sum_i d_i^2)(\sum_i d_i^3)}}{\sum_i d_i} \sqrt{s\tilde{g}}/\nu \quad (45)$$

a quantity similar to the Galileo number. From Eq. (44), one obtains the nondimensionalized settling velocity  $\tilde{v}_s$  of a single composite grain in quiescent fluid ( $\epsilon = 1$ ) as (45)

$$\tilde{v}_s = \left[ \sqrt{\frac{1}{4} \left[ \left( \frac{\Re_c}{C_D^\infty \widetilde{Ga}} \right)^2 + \frac{4}{3C_D^\infty} - \frac{1}{2} \sqrt{\frac{\Re_c}{C_D^\infty \widetilde{Ga}}} \right]} \right]^m \quad (46)$$

and subsequently the drag coefficient as

$$C_D = \frac{4(s-1)gd}{3v_s^2} = \frac{4}{3\tilde{v}_s^2}. \quad (47)$$

Here we used that a composite grain is treated as if the projected area of all its component spheres is always, regardless of its orientation relative to the flow, fully exposed to the flow, which follows from Eq. (43). That is, the total projected area seen by the flow,  $A_p = \frac{\pi}{4} \sum_i d_i^2$ , is constant, and therefore  $A_p^{\text{eff}} = A_p^{\text{max}}$ .

**Sphere-normalized drag coefficient after Deal et al. (14)** Deal et al. (14) defined the sphere-normalized drag coefficient  $C^*$  as

$$C^* \equiv S_f v_o^2 / v_s^2, \quad (48)$$

where  $v_o$  is the theoretical value of the settling velocity of spheres, given by (14, 62)

$$v_{o*} = -3.81564 + 1.94593D_* - 0.09016D_*^2 - 0.00855D_*^3 + 0.00075D_*^4, \quad (49)$$

with  $v_{o*} \equiv \log_{10} v_o^3 / [(s-1)g\nu]$ ,  $D_* \equiv \log_{10}(s-1)gd_o^3/\nu^2$ , and  $d_o$  the volume-equivalent sphere diameter (note that  $d_o \neq d = c_g$ ).

## Determinations of angle of repose and its uncertainty

We acquired the same spheres as those used in Ref. (15) (NC18EXP in Table 1) from the same company (Chiao Dar Acry & Advertisement Co., Ltd., <http://www.bridgeacry.com.tw>) and measured  $\mu_s$  using the funnel method (48) in the manner described in Ref. (14) (Fig. 8). Furthermore, we confirmed with DEM simulations that different measurement methods have only a small effect on  $\mu_s$  provided that a sufficiently large number of grains is used and that there is some means of preventing grains from rolling away (such as a rim or a rough bed, see Fig. 9). Based on these simulations, we assign an uncertainty of 5% to all  $\mu_s$ -measurements, including those from different studies and methods.

## Contact parameters and $\mu_s$ in grain-unresolved CFD-DEM simulations

Table 3 summarizes the contact parameters in the grain-unresolved simulation.

## References

1. V. Poggiali, M. Mastrogiuseppe, A. G. Hayes, R. Seu, S. P. D. Birch, R. Lorenz, C. Grima, J. D. Hofgartner, Liquid-filled canyons on titan. *Geophysical Research Letters* **43**, 7887-7894 (2016).
2. F. Charru, B. Andreotti, P. Claudin, Sand ripples and dunes. *Annual Review of Fluid Mechanics* **45**, 469-493 (2013).
3. O. Durán Vinent, B. Andreotti, P. Claudin, C. Winter, A unified model of ripples and dunes in water and planetary environments. *Nature Geoscience* **12**, 345-350 (2019).
4. V. R. Baker, C. W. Hamilton, D. M. Burr, V. C. Gulick, G. Komatsu, W. Luo, J. W. Rice, J. Rodriguez, Fluvial geomorphology on Earth-like planetary surfaces: A review. *Geomorphology* **245**, 149-182 (2015).
5. J. Schieber, Mud re-distribution in epicontinental basins – Exploring likely processes. *Marine and Petroleum Geology* **71**, 119-133 (2016).
6. A. Shchepetkina, M. K. Gingras, M. G. Mángano, L. A. Buatois, Fluvio-tidal transition zone: Terminology, sedimentological and ichnological characteristics, and significance. *Earth-Science Reviews* **192**, 214-235 (2019).
7. A. Recking, A comparison between flume and field bed load transport data and consequences for surface-based bed load transport prediction. *Water Resources Research* **46**, W03518 (2010).



8. C. Ancey, A. Recking, Scaling behavior of bedload transport: what if bagnold was right? *Earth-Science Reviews* **246**, 104571 (2023).
9. B. Dhont, C. Ancey, Are bedload transport pulses in gravel bed rivers created by bar migration or sediment waves? *Geophysical Research Letters* **45**, 5501-5508 (2018).
10. E. M. Yager, J. G. Venditti, H. J. Smith, M. W. Schmeeckle, The trouble with shear stress. *Geomorphology* **323**, 41-50 (2018).
11. J. Guo, Sidewall and non-uniformity corrections for flume experiments. *Journal of Hydraulic Research* **53**, 218-229 (2015).
12. Q. Zhang, E. Deal, J. T. Perron, J. G. Venditti, S. J. Benavides, M. Rushlow, K. Kamrin, Fluid-driven transport of round sediment particles: From discrete simulations to continuum modeling. *Journal of Geophysical Research: Earth Surface* **127**, e2021JF006504 (2022).
13. Q. Zhang, E. Deal, J. T. Perron, J. G. Venditti, S. J. Benavides, M. Rushlow, K. Kamrin, Discrete simulations of fluid-driven transport of naturally shaped sediment particles. *ESS Open Archive* (2023).
14. E. Deal, J. G. Venditti, S. J. Benavides, R. Bradley, Q. Zhang, K. Kamrin, J. T. Perron, Grain shape effects in bed load sediment transport. *Nature* **613**, 298-302 (2023).
15. W. J. Ni, H. Capart, Stresses and drag in turbulent bed load from refractive index-matched experiments. *Geophysical Research Letters* **45**, 7000-7009 (2018).
16. G. Gioia, F. A. Bombardelli, Scaling and similarity in rough channel flows. *Physical Review Letters* **88**, 014501 (2002).
17. G. Gioia, Pinaki Chakraborty, Turbulent friction in rough pipes and the energy spectrum of the phenomenological theory. *Physical Review Letters* **96**, 044502 (2006).

18. T. Pähtz, O. Durán, Universal friction law at granular solid-gas transition explains scaling of sediment transport load with excess fluid shear stress. *Physical Review Fluids* **3**, 104302 (2018).
19. H. A. Einstein, Formulas for the transportation of bedload. *Transactions of ASCE* **107**, 561-597 (1942).
20. J. W. Johnson, The importance of considering sidewall friction in bed-load investigations. *Civil Engineering* **12**, 329-332 (1942).
21. J. Guo, Exact procedure for Einstein-Johnson's sidewall correction in open channel flow. *Journal of Hydraulic Engineering* **143**, 06016027 (2017).
22. T. Pähtz, O. Durán, Unification of aeolian and fluvial sediment transport rate from granular physics. *Physical Review Letters* **124**, 168001 (2020).
23. C. Ancey, Bedload transport: a walk between randomness and determinism. Part 1. The state of the art. *Journal of Hydraulic Research* **58**, 1-17 (2020).
24. P. Frey, M. Dufresne, T. Böhm, M. Jodeau, C. Ancey, *River Flow 2006* (Taylor & Francis Group, London, UK, 2006), pp. 887–893.
25. P. Frey, Particle velocity and concentration profiles in bedload experiments on a steep slope. *Earth Surface Processes and Landforms* **39**, 646-655 (2014).
26. A. Armanini, V. Cavedon, Bed-load through emergent vegetation. *Advances in Water Resources* **129**, 250-259 (2019).
27. V. Carrillo, J. Petrie, L. Timbe, E. Pacheco, W. Astudillo, C. Padilla, F. Cisneros, Validation of an experimental procedure to determine bedload transport rates in steep channels with coarse sediment. *Water* **13**, 672 (2022).

28. R. Jain, S. Tschisgale, J. Fröhlich, Impact of shape: Dns of sediment transport with non-spherical particles. *Journal of Fluid Mechanics* **916**, A38 (2021).
29. A. G. Kidanemariam, M. Uhlmann, Formation of sediment patterns in channel flow: minimal unstable systems and their temporal evolution. *Journal of Fluid Mechanics* **818**, 716-743 (2017).
30. R. Zhu, Z. He, K. Zhao, B. Vowinckel, E. Meiburg, Grain-resolving simulations of submerged cohesive granular collapse. *Journal of Fluid Mechanics* **942**, A49 (2022).
31. D. Rebai, D. Berzi, F. Ballio, V. Matousek, Experimental comparison of inclined flows with and without intense sediment transport: Flow resistance and surface elevation. *Journal of Hydraulic Engineering* **148**, 04022026 (2022).
32. R. Maurin, J. Chauchat, P. Frey, Revisiting slope influence in turbulent bedload transport: consequences for vertical flow structure and transport rate scaling. *Journal of Fluid Mechanics* **839**, 135-156 (2018).
33. R. Monthiller, Particle shape influence on turbulent bedload transport, Master's thesis, EN-SEEIHT, University of Toulouse, Toulouse, France (2019).
34. S. Q. Yang, S. Y. Lim, J. A. McCorquodale, Investigation of near wall velocity in 3-d smooth channel flows. *Journal of Hydraulic Research* **43**, 149-157 (2005).
35. R. Jain, S. Tschisgale, J. Fröhlich, Effect of particle shape on bedload sediment transport in case of small particle loading. *Meccanica* **55**, 299-315 (2020).
36. T. Song, Velocity and turbulence distribution in nonuniform and unsteady open-channel flow, Ph.D. thesis, Swiss Federal Institute of Technology EPFL, Lausanne, Switzerland (1994).

37. T. Song, Y. M. Chiew, Turbulence measurement in non-uniform open-channel flow using acoustic Doppler velocimeter (ADV). *Journal of Engineering Mechanics* **127**, 219-232 (2001).
38. C. Auel, I. Albayrak, R. M. Boes, Turbulence characteristics in supercritical open channel flows: Effects of froude number and aspect ratio. *Journal of Hydraulic Engineering* **140**, 04014004 (2014).
39. E. Deal, J. G. Venditti, S. J. Benavides, R. Bradley, Q. Zhang, K. Kamrin, J. T. Perron, Addendum: Grain shape effects in bed load sediment transport. *Nature* **623**, E21 (2023).
40. J. Chauchat, A comprehensive two-phase flow model for unidirectional sheet-flows. *Journal of Hydraulic Research* **56**, 15-28 (2018).
41. F. Boyer, É. Guazzelli, O. Pouliquen, Unifying suspension and granular rheology. *Physical Review Letters* **107**, 188301 (2011).
42. T. Pähtz, O. Durán, The cessation threshold of nonsuspended sediment transport across aeolian and fluvial environments. *Journal of Geophysical Research: Earth Surface* **123**, 1638-1666 (2018).
43. R. A. Bagnold, The flow of cohesionless grains in fluid. *Philosophical Transactions of the Royal Society London A* **249**, 235-297 (1956).
44. A. H. Clark, M. D. Shattuck, N. T. Ouellette, C. S. O'Hern, Role of grain dynamics in determining the onset of sediment transport. *Physical Review Fluids* **2**, 034305 (2017).
45. T. Pähtz, Y. Liu, Y. Xia, P. Hu, Z. He, K. Tholen, Unified model of sediment transport threshold and rate across weak and intense subaqueous bedload, windblown sand, and

- windblown snow. *Journal of Geophysical Research: Earth Surface* **126**, e2020JF005859 (2021).
46. W. S. Chepil, The use of evenly spaced hemispheres to evaluate aerodynamic forces on a soil surface. *Transcripts of the American Geophysical Union* **39**, 397-403 (1958).
  47. W. S. Chepil, The use of spheres to measure lift and drag on wind-eroded soil grains. *Soil Science Society of America Journal* **25**, 343-345 (1961).
  48. H. M. Beakawi Al-Hashemi, O. S. Baghabra Al-Amoudi, A review on the angle of repose of granular materials. *Powder Technology* **330**, 397-417 (2018).
  49. V. Matoušek, Š. Zrostlík, Collisional transport model for intense bed load. *Journal of Hydrology and Hydromechanics* **68**, 60-69 (2020).
  50. O. Durán, B. Andreotti, P. Claudin, Numerical simulation of turbulent sediment transport, from bed load to saltation. *Physics of Fluids* **24**, 103306 (2012).
  51. R. Maurin, J. Chauchat, B. Chareyre, P. Frey, A minimal coupled fluid-discrete element model for bedload transport. *Physics of Fluids* **27**, 113302 (2015).
  52. J. Xie, P. Hu, T. Pähtz, Z. He, N. Cheng, Fluid-particle interaction regimes during the evolution of turbidity currents from a coupled les/dem model. *Advances in Water Resources* **163**, 104171 (2022).
  53. F. J. Moraga, F. J. Bonetto, R. T. Lahey, Lateral forces on spheres in turbulent uniform shear flow. *International Journal of Multiphase Flow* **25**, 1321-1372 (1999).
  54. X. Li, S. Balachandar, H. Lee, B. Bai, Fully resolved simulations of a stationary finite-sized particle in wall turbulence over a rough bed. *Physical Review Fluids* **4**, 094302 (2019).

55. P. L. Wiberg, J. D. Smith, Calculations of the critical shear stress for motion of uniform and heterogeneous sediments. *Water Resources Research* **23**, 1471-1480 (1987).
56. S. J. Benavides, E. Deal, J. G. Venditti, R. Bradley, Q. Zhang, K. Kamrin, J. T. Perron, How fast or how many? Sources of intermittent sediment transport. *Geophysical Research Letters* **50**, e2022GL101919 (2023).
57. T. Pächtz, K. Tholen, General average balance equations for a mixture of rigid particles and a continuous fluid. *arXiv:2308.09661v2* (2024).
58. A. G. Kidanemariam, The formation of patterns in subaqueous sediment, Ph.D. thesis, Karlsruhe Institute of Technology, Karlsruhe, Germany (2016).
59. R. Antonia, B. Pearson, Reynolds number dependence of velocity structure functions in a turbulent pipe flow. *Flow, Turbulence and Combustion* **64**, 95-117 (2000).
60. H. Tennekes, J. L. Lumley, *A First Course in Turbulence* (MIT Press, Cambridge, MA, 1972).
61. R. Sun, H. Xiao, H. Sun, Realistic representation of grain shapes in CFD-DEM simulations of sediment transport with a bonded-sphere approach. *Advances in Water Resources* **107**, 421-438 (2017).
62. W. E. Dietrich, Settling velocity of natural particles. *Water Resources Research* **18**, 1615-1626 (1982).
63. F. Elekesa, E. J. R. Parteli, An expression for the angle of repose of dry cohesive granular materials on earth and in planetary environments. *Proceedings of the National Academy of Sciences of the United States of America* **118**, e2107965118 (2021).

**Acknowledgements:** The authors thank Yesheng Lu for helping finding grain-shape-controlled bedload transport data sets.

**Funding:**

National Natural Science Foundation of China 12350710176 (T.P.)

National Natural Science Foundation of China 12272344 (T.P.)

National Natural Science Foundation of China 52171276 (Z.H.).

Texas A&M Engineering Experiment Station (O.D.).

**Author Contributions** T.P., O.D., K.T. designed and conceptualized the study. T.P., Y.C., K.T., O.D. developed the methods and models. T.P., Y.C., O.D., J.X. analyzed the data. T.P., Y.C., O.D. conducted the simulations behind the data sets BLRANSx. J.X., Y.C. conducted the simulations behind the data sets LESx. Ré.M. conducted the simulations behind the data sets M19RANSx. Ra.M. conducted the simulations behind the data set M18RANS. Y.-C.L. and H.-C.H measured  $\mu_s$  for the data set NC18EXP. J.X., Y.C. numerically studied the sensitivity of  $\mu_s$  to its method of determination. T.P., O.D., P.H., Z.H., Ra.M. supervised the study. T.P., Y.C. wrote the initial and revised drafts. All authors reviewed and edited the drafts.

**Competing Interests** Authors declare that they have no competing financial interests.

**Data and materials availability:** The data required to reproduce Figs. 1A-1E, 3, 4, 5, and 7, and a Matlab code to plot them are available online at <https://doi.org/10.5281/zenodo.13317930>. The measurements of  $\mu_s$  resulting from the experiment in Fig. 8 and simulations in Fig. 9 are reported in Table 1. The data plotted in Fig. 1F are from the tables of Ref. (11). The data plotted in Figs. 2 and 6A are from the supplementary materials of Ref. (15). The data plotted in Figs. 6B and 6C are from the tables and supplementary materials of Ref. (31).

Experimental or numerical study	Width-depth ratio, $b/h$	Grain shape	Shape parameters			Hydrodynamic conditions			
			$S_f$	$C_D$	$\mu_s$	$s$	$Ga$	$\alpha$	$h^*$
D23EXPs (14)	0.09–0.16	spheres	1	0.43	0.46	2.57	1334–1339	0.03–0.13	13–24
D23EXPe (14)	0.10–0.14	ellipsoids	0.83	0.60	0.60	2.42	1312–1314	0.03–0.09	15–22
D23EXPe (14)	0.10–0.13	chips	0.51	0.39	0.65	2.36	767–768	0.04–0.08	22–29
D23EXPg (14)	0.10–0.15	gravel	0.68	0.54	0.78	2.48	733–735	0.04–0.11	20–32
D23EXPe (14)	0.09–0.12	prisms	0.88	0.79	0.86	2.40	725	0.03–0.06	26–35
NC18EXP (15)	5.2–7.5	spheres	1	0.49	0.45	1.39	998	0.02–0.03	2.3–3.3
R22EXPe (31)	5.5–5.6	cylinders	0.84	0.32	0.60	1.42	738	0.05–0.06	8.4–14
R22EXPl (31)	5.0–5.8	lenses	0.55	0.45	0.62	1.37	196	0.03–0.05	16–18
Z22LESn (12)	0.15–0.16	spheres	1	0.48	0.45	2.55	1354–1357	0.04–0.10	13–14
Z23LES (13)	0.09–0.10	gravel	0.67	0.71	0.75	2.47	718–719	0.03–0.10	32–33
Z22LESw (12)	$\infty$	spheres	1	0.48	0.45	2.55	1378	0.01–0.03	4.6–22
J21DNS (28)	$\infty$	spheres	1	N/A	N/A	2.55	44.7	0 ( $\chi > 0$ )	$\approx 18$
KU17DNS (29)	$\infty$	spheres	1	N/A	N/A	2.5	28.37	0 ( $\chi > 0$ )	$\approx 13$
M18RANS (32)	$\infty$	spheres	1	0.42	0.40	1.75–4	1259–2521	0.01–0.19	2.0–62
M19RANSs (33)	$\infty$	spheres	1	0.42	0.49	2.5	1782	0.05	4.1–18
M19RANSSt1 (33)	$\infty$	triplets	0.85	0.42	0.55	2.5	1782	0.05	6.1–26
M19RANSSt2 (33)	$\infty$	triplets	0.75	0.42	0.63	2.5	1782	0.05	8.0–33
M19RANSSt3 (33)	$\infty$	triplets	0.71	0.42	0.68	2.5	1782	0.05	9.9–40
M19RANSSt4 (33)	$\infty$	triplets	0.62	0.42	0.72	2.5	1782	0.05	12–47
M19RANSSt5 (33)	$\infty$	triplets	0.58	0.42	0.69	2.5	1782	0.05	14–55
LES	$\infty$	spheres	1	0.54	0.49	2.56	1341	0 ( $\chi > 0$ )	18–22
LESCD	$\infty$	spheres	1	1.78	0.49	2.56	1341	0 ( $\chi > 0$ )	20–23
BLRANS1	$\infty$	spheres	1	2.24	0.38	[1.1, 2.65]	50	0–0.16	$\infty$
BLRANS2	$\infty$	spheres	1	1.46	0.38	[1.1, 2.65]	100	0	$\infty$
BLRANS2CD	$\infty$	spheres	1	15.9	0.38	2.65	50	0	$\infty$

Table 1: **Summary of bedload flux data shown in this study.** The top, middle, and bottom entries correspond to experiments, grain-resolved CFD-DEM simulations, and grain-unresolved CFD-DEM simulations, respectively. Those data of the data sets BLRANS1 and BLRANS2 with  $s = 2.65$  and  $\alpha = 0$  are from Ref. (22). Note that the here listed values of  $C_D$ ,  $Ga$ , and  $h^*$  for the data of Refs. (12–14) (Z22LESx, Z23LES, D23EXPx, where ‘x’ stands for an arbitrary character) can differ from those reported in these references due to a different definition of  $d$ .



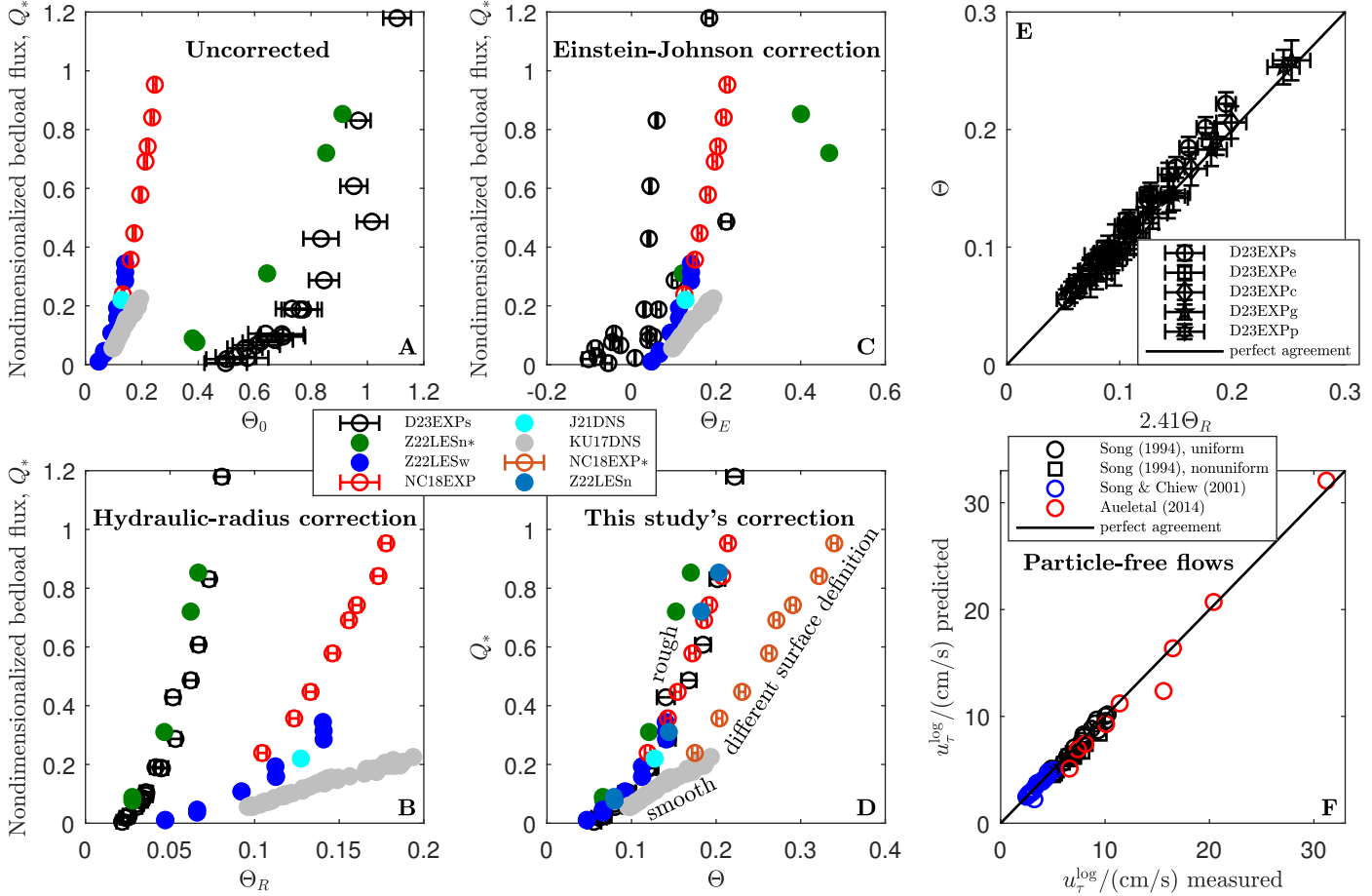


**Figure 1: Channel geometry corrections.** (A-D) Nondimensionalized bedload flux  $Q_*$  versus Shields numbers for spherical grains: (A) uncorrected for sidewall effects ( $\Theta_0$ ), (B) hydraulic-radius correction (11) ( $\Theta_R$ ), (C) Einstein-Johnson correction (19–21) ( $\Theta_E$ ), (D) our universal correction ( $\Theta$ ). Symbols correspond to data from experiments and grain-resolved simulations (Table 1). An error bar indicates the standard error and/or uncertainty range. In the absence of error bars, uncertainties are smaller than the symbol size. Except for KU17DNS ( $s^{1/2}Ga \simeq 44.86$ , smooth), all data are in the rough regime ( $s^{1/2}Ga > 70$ ). Z22LESw and NC18EXP are based on a granular-physics-based bed surface definition (18) (Methods) and NC18EXP\* on these authors’ original definition (15). For all other data sets, reported values of the flow depth  $h$  are used as it has a negligible effect on the Shields numbers. Z22LESn\* refers to unmodified data, whereas for Z22LESn in (D), the sidewall correction, and thus  $\Theta$ , has been modified to account for the fact that the grid resolution of the grain-resolved LES simulations behind these data was limited to 15 times the Kolmogórov length scale (see text). (E)  $\Theta$  versus  $2.41\Theta_R$ , based on  $\tau_b = 2.41\tau_R$ , the empirical correction Deal et al. (14) obtained from fitting log-profiles to flow velocity data. For their data sets for non-spherical grains,  $d = c_g$  is used in the rescaling of these Shields numbers. (F) Log-profile shear velocity  $u_\tau^{\log} \simeq \sqrt{\tau_b/\rho_f}$  (Methods) predicted by our sidewall correction versus measured one for experimental data from particle-free flows in open channels consisting of rough beds and smooth sidewalls (36–38) (data as summarized in the tables of Ref. (11)). For nonuniform flows, the bed slope  $\tan \alpha$  is corrected using Eq. (1b) of Ref. (11). The roughness sizes are  $r = c_g/2$  for the experiments of Ref. (36) (water-worked bed),  $r = d_0$  for those of Ref. (37) (sand grains glued on aluminum plate), and  $r = k$  for those of Ref. (38) (with  $k$  the measured absolute roughness).

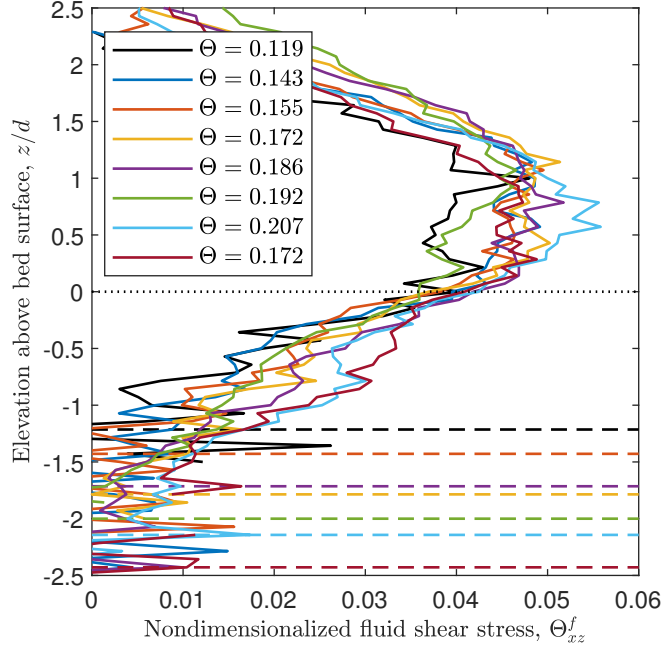


Figure 2: **Independent evidence supporting our bed surface elevation definition.** Vertical profiles (solid lines) of the nondimensionalized fluid shear stress  $\Theta_{xz}^f \equiv \tau_{xz}^f / (\rho_p \tilde{g}_z d)$  for the data set NC18EXP (15). The data exhibit a focal point at the bed surface elevation  $z = 0$  (defined as described in Methods):  $\Theta_{xz}^f(0) \approx 0.04$ , a property required for a bed surface definition to be physically meaningful (18). The fluid shear stress  $\tau_{xz}^f$  (Methods) is calculated from local quantities at the channel center as described in Chauchat (40), assuming that the mixture viscosity obeys the closure measured by Boyer et al. (41) for viscous suspensions. The dashed lines correspond to the bed surface elevations determined by Ni and Capart (15).

Numerical model	$\mathfrak{R}_c$	$C_D^\infty$	$m$	$p_1$	$p_2$
Maurin et al. (51)	24.4	0.4	1	3.1	3.1
Durán et al. (50) (nominal)	24	0.5	2	0	0
Durán et al. (50) (enhanced drag)	96	2	2	0	0
Xie et al. (52) (nominal)	23.04	0.3969	2	$p$	$p - 1$
Xie et al. (52) (enhanced drag)	69.12	1.1907	2	$p$	$p - 1$

Table 2: **Summary of drag law parameters used in grain-unresolved CFD-DEM simulations of bedload transport.** The exponent  $p$  is given by  $p = 3.7 - 0.65 \exp[-(1.5 - \log_{10}(\epsilon |\mathbf{u}_r| d_i / \nu))^2 / 2]$ .

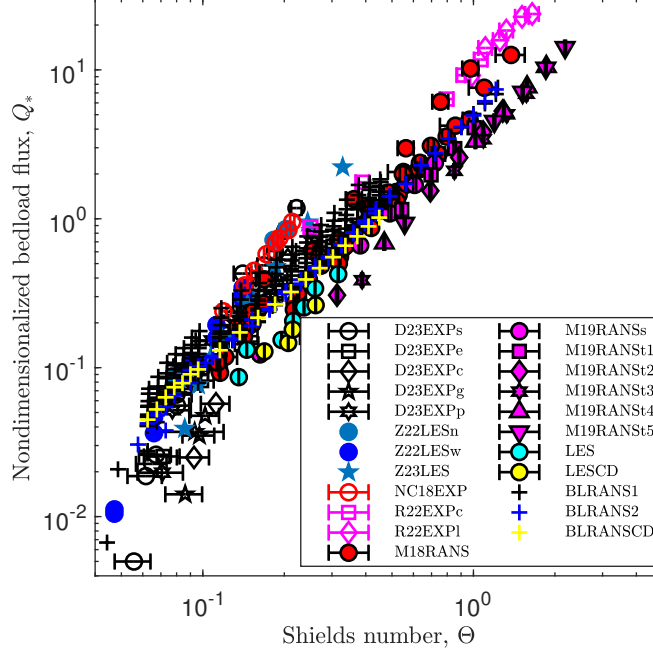


Figure 3: **Entire data compilation.** Nondimensionalized bedload flux  $Q_*$  versus Shields number  $\Theta$ , both rescaled using the generalized grain diameter definition  $d \equiv \frac{3}{2}V_p/A_p^{\max}$  (see text). Symbols correspond to data from a variety of experimental and numerical methods (Table 1). An error bar indicates the standard error and/or uncertainty range. In the absence of error bars, uncertainties are smaller than the symbol size.

Numerical model	$e_n$	$\mu_c$	$\mu_s$
Maurin et al. (51) (data from Ref. (32))	0.5	0.4	0.40
Maurin et al. (51) (data from Ref. (33))	0.5	0.5	0.49–0.72
Durán et al. (50)	0.9	0.5	0.38
Xie et al. (52)	0.3	0.5	0.49

Table 3: **Contact model parameters.** Normal restitution coefficient  $e_n$  and tangential contact friction coefficient  $\mu_c$  used in grain-unresolved CFD-DEM simulations of bedload transport. The tangent of the static angle of repose,  $\mu_s$ , has been determined as described in Fig. 9.

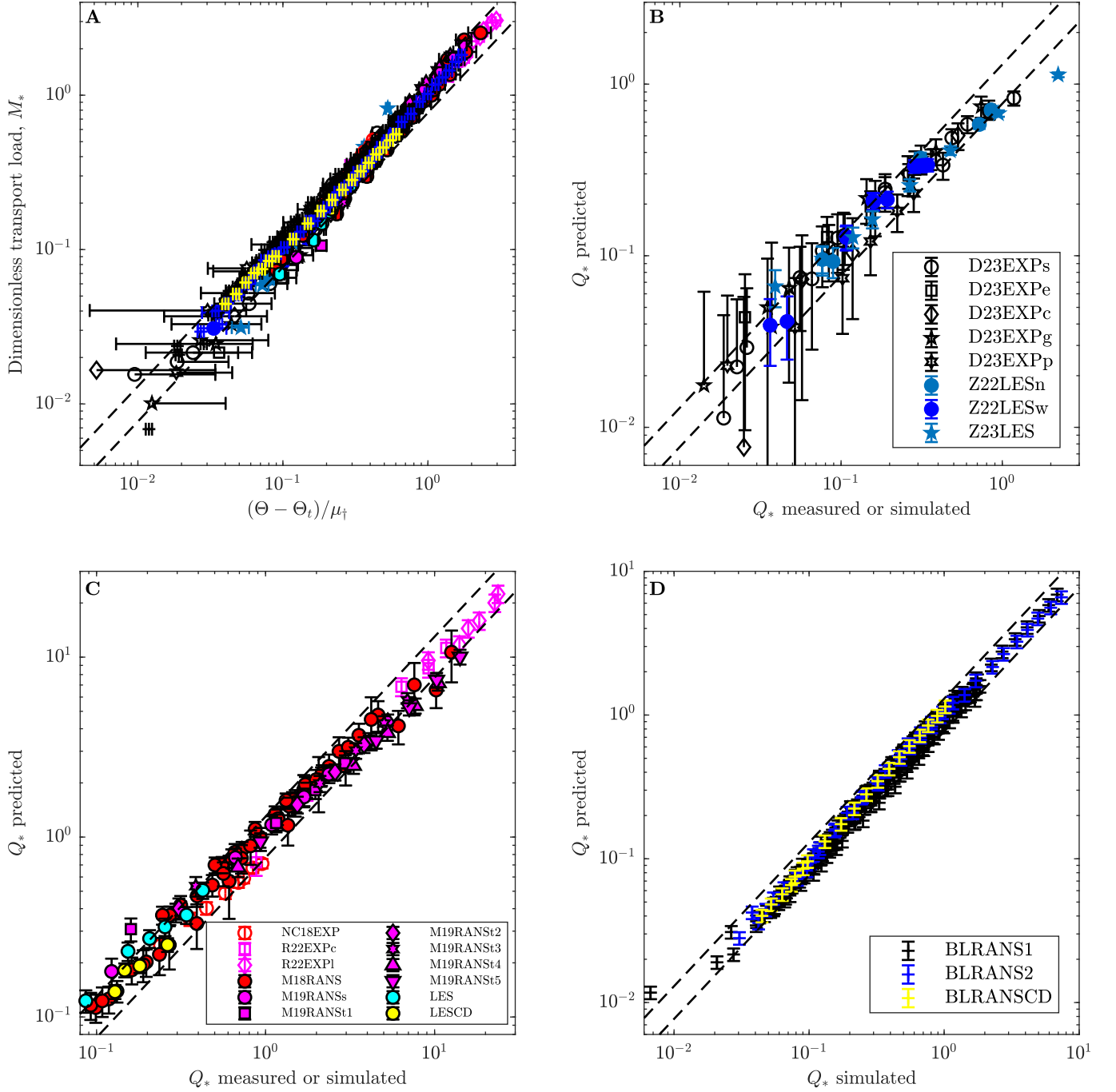
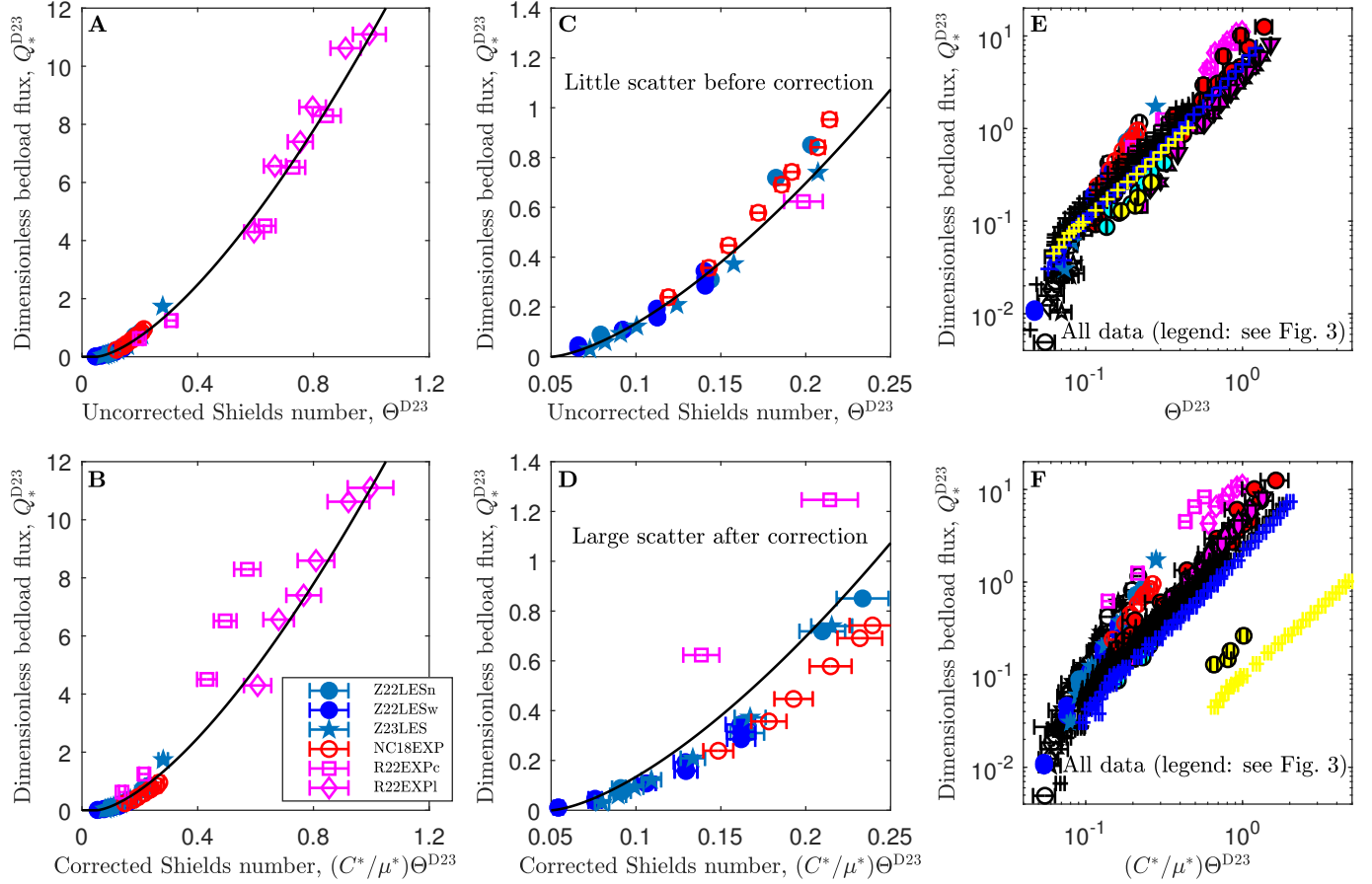


Figure 4: **Test of our rough-bedload flux model across grain shapes, bed slopes, flow strengths, and flow depths.** (A) Nondimensionalized transport load  $M_*$ , calculated from the  $Q_*$ -data via Eq. (4), versus  $(\Theta - \Theta_t)/\mu_\dagger$ . (B-D)  $Q_*$  predicted by Eqs. (4) and (6) versus measured or simulated  $Q_*$ . Symbols correspond to data from a variety of methods (Table 1). An error bar indicates the standard error and/or uncertainty range. In the absence of error bars, uncertainties are smaller than the symbol size. When  $s^{1/4}Ga \geq 200$ ,  $\Theta_t$  is calculated by Eq. (7). Otherwise (only BLRANSx),  $\Theta_t$  is determined directly from the simulations, as described in Ref. (22). All grain-unresolved simulations neglect lift forces, implying  $\overline{f_L}/\overline{f_D} = 0$ . Almost all data fall within a factor of 1.3 of the model prediction, delineated by the dashed lines.



**Figure 5: Test of Deal et al.'s (14) bedload flux model with independent data.** Nondimensionalized bedload flux  $Q_*^{D23}$  versus shape-uncorrected Shields number  $\Theta^{D23}$  (A, C, E) and shape-corrected Shields number  $(C^*/\mu^*)\Theta^{D23}$  (B, D, F), based on the same definitions as Deal et al. (14). Symbols in (A-D) correspond to data from experiments and grain-resolved simulations from independent studies (Table 1). Symbols in (E, F) correspond to the entire data compilation, including D23EXPx (14) and data from grain-unresolved simulations. An error bar indicates the standard error and/or uncertainty range. In the absence of error bars, uncertainties are smaller than the symbol size. The solid lines correspond to  $Q_*^{D23} = 12(\Theta^{D23} - 0.05)^{3/2}$  (A, C) and  $Q_*^{D23} = 12(\Theta^{D23} C^*/\mu^* - 0.05)^{3/2}$  (B, D). The latter is the prediction by Deal et al. (14).

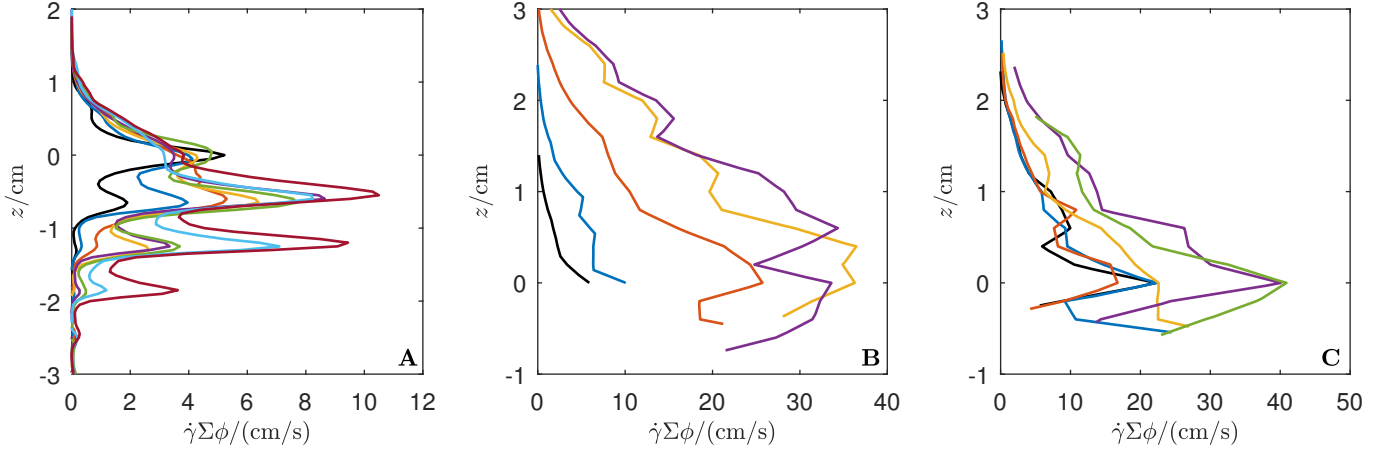


Figure 6: **Determination of bed surface elevation for experimental wide-channel data sets.** Vertical profiles of  $\dot{\gamma}\Sigma\phi$  for the data sets (A) NC18EXP (15), (B) R22EXPC (31), and (C) R22EXPI (31) (Table 1). They are used to determine the bed surface elevation  $z = 0$  in the manner described in the text.

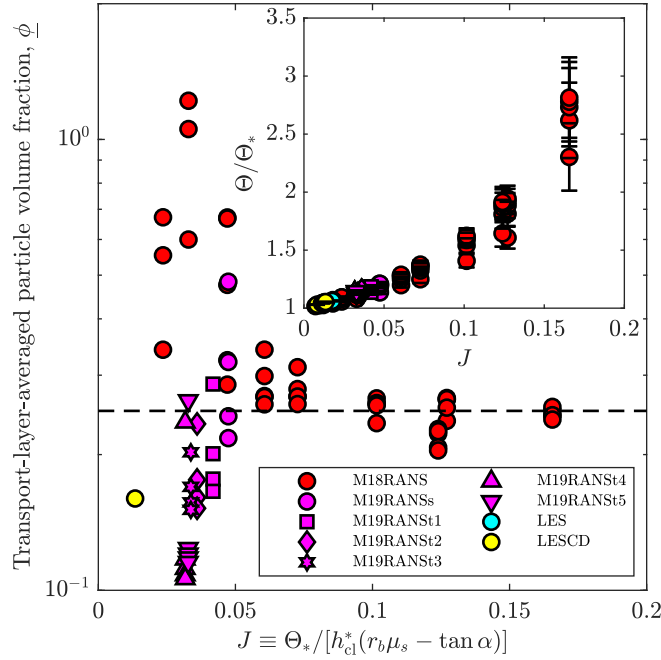


Figure 7: **Determination of transport-layer-averaged particle volume fraction  $\phi_{\perp}$ .**  $\phi_{\perp}$  calculated from the  $Q_*$ -data as described in the text, versus  $J$ . Symbols correspond to grain-unresolved CFD-DEM simulations (Table 1). The dashed line indicates the value  $\phi_{\perp} = 0.25$  exhibited for large  $J$ , where the ratio  $\Theta/\Theta_*$  deviates from unity the most. Inset: Estimate of  $\Theta/\Theta_*$  resulting from  $\phi_{\perp} = 0.25$ , where the error bars correspond to the propagated uncertainty of  $\mu_s$ , required for predicting  $M_*$  and therefore  $\Theta$ , as described in the text.

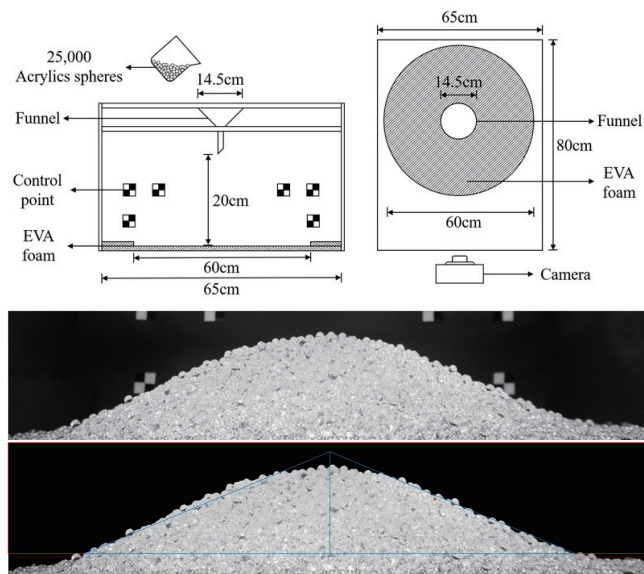


Figure 8: **Measurements of  $\mu_s$  for the data set NC18EXP (Table 1).** We slowly poured 25,000 grains onto an elevated disk bounded by a  $2d$ -high rim. The angle of repose of the resulting heap is then determined as the base angle of the isosceles triangle that has the same area as the projected heap, averaged over two side-view images separated by a rotation of  $90^\circ$  (63).

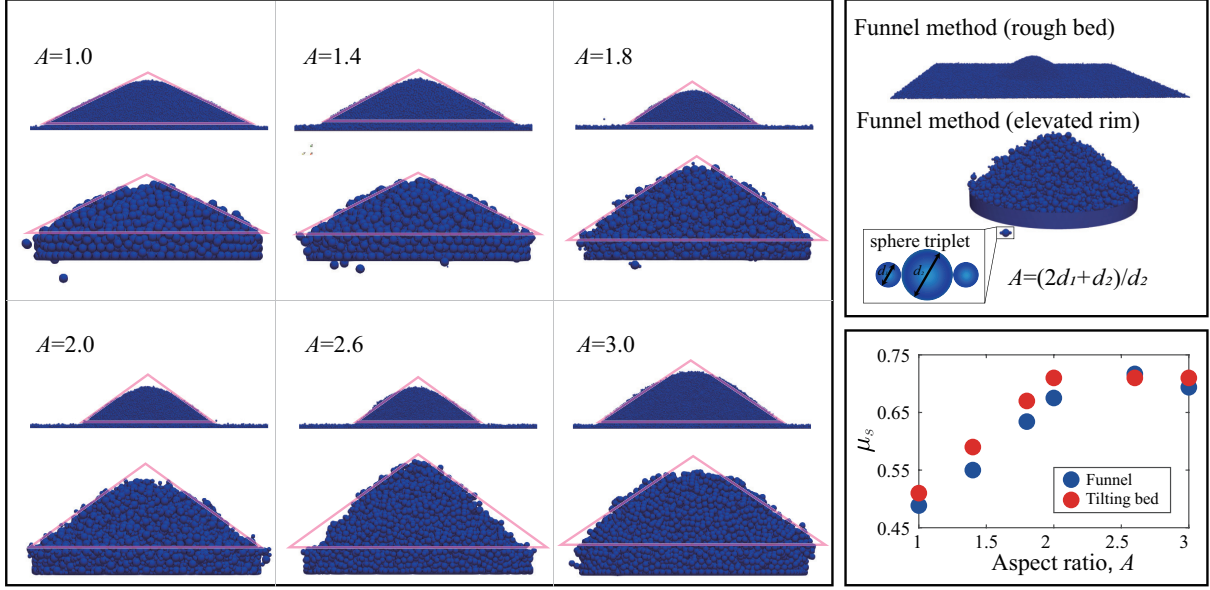


Figure 9: **Numerical determination of the static angle of repose.** We compare three different methods of measuring the tangent of the static angle of repose,  $\mu_s$ , for the composite grains (spheres and sphere triplets) used in the grain-unresolved DEM-CFD simulations: slowly pouring a sufficient number of grains onto a rough bed consisting of spheres of the same volume-equivalent sphere diameter  $d_0$  (funnel method 1), onto an elevated disk of diameter  $24d_0$  bounded by a  $2d_0$ -high rim (funnel method 2, exactly as described in Ref. (14)), and tilting the granular bed until the granular bulk moves (tilting method). The most reliable and reproducible results are yielded by funnel method 1, where the angle of repose is determined as the base angle of the isosceles triangle that has the same area as the projected heap, averaged over two side-view images separated by a rotation of  $90^\circ$  (63). For funnel method 2, the heaps exhibit too irregular shapes when the aspect ratio  $A$  becomes too large, making a clear determination of the angle of repose difficult. However, for  $A \lesssim 2$ , it yields values very close to funnel method 1. The tilting method also yields similar results as funnel method 1, though it is sometimes difficult to distinguish between bulk and isolated-grain motion. We therefore decided to use funnel method 1 as the standard procedure to determine  $\mu_s$  in the grain-unresolved DEM-CFD simulations.